Restoration of locomotor function following stimulation of the A13 region in Parkinson's mouse models.

Linda H Kim[1,2]*, Adam Lognon[1,2]*, Sandeep Sharma[1,3], Michelle A. Tran[3], Taylor Chomiak[1,4], Stephanie Tam[3], Claire McPherson[3], Shane E. A. Eaton[1,3], Zelma H. T. Kiss[1,2,4], Patrick J. Whelan[#1,3]
*These authors contributed equally.

Affiliations: [1]Hotchkiss Brain Institute, University of Calgary, Calgary, AB, Canada, T2N4N1, [2]Department of Neuroscience, University of Calgary, Calgary, AB, Canada, T2N 4N1, [3]Faculty of Veterinary Medicine, University of Calgary, Calgary, AB, Canada, T2N4N1, [4]Department of Clinical Neurosciences, University of Calgary, Calgary, AB, Canada, T2N 4N1

[#] **Corresponding author**
Patrick J. Whelan
HMRB 168,
3330 Hospital Drive NW,
University of Calgary
Calgary, AB
T2N 4N1
Email: whelan@ucalgary.ca

Short Title: Zona incerta mediated recovery of PD function

Author Contributions: LHK and AL performed experiments and prepared figures. MAT and PJW edited figures. LHK, AL, ZHT and PJW conceived and designed the research and interpreted the results. PJW procured funding for the experiments. SS and AL performed surgeries for lesions, optogenetic experiments and conducted behavioral experiments. LHK and SEAE optimized light-sheet imaging. MAT, ST, and CM performed manual cell counting. TC performed analysis and prepared figures on gait analysis. LHK, AL, TC, ZHT, and PJW drafted the manuscript. All authors reviewed and approved the final version of the manuscript.

Competing Interest Statement: None.

Keywords: Dopamine, Connectome, Parkinson's Disease, Motor.

ABSTRACT

Parkinson's disease (PD) is characterized by extensive motor and non-motor dysfunction, including gait disturbance, which is difficult to treat effectively. This study explores the therapeutic potential of targeting the A13 region, a dopamine-containing area of the medial zona incerta (mZI) that has shown relative preservation in PD models. The A13 is identified to project to the mesencephalic locomotor region (MLR), with a subpopulation of cells displaying activity correlating to movement speed, suggesting its potential involvement in locomotor function. We show that photoactivation of this region can alleviate bradykinesia and akinetic symptoms in a mouse model of PD, revealing the presence of preserved parallel motor pathways for movement. We identified areas of preservation and plasticity within the mZI connectome using whole-brain imaging. Our findings suggest a global remodeling of afferent and efferent projections of the A13 region, highlighting the zona incerta's role as a crucial hub for the rapid selection of motor function. Despite endogenous compensatory mechanisms proving insufficient to overcome locomotor deficits in PD, our data demonstrate that photostimulation of the A13 region effectively restores locomotor activity. The study unveils the significant pro-locomotor effects of the A13 region and suggests its promising potential as a therapeutic target for PD-related gait dysfunction.

SIGNIFICANCE STATEMENT

This work examines the function of the A13 nucleus in locomotion, an area with direct connectivity to locomotor regions in the brainstem. Our work shows that A13 stimulation can restore locomotor function and improve bradykinesia symptoms in a PD mouse model.

INTRODUCTION

Parkinson's disease (PD) is a complex condition affecting many facets of motor and non-motor functions, including visual, olfactory, memory and executive functions (Cenci and Björklund, 2020). Due to the widespread features of PD, focusing on changes within a single pathway cannot account for all symptoms. Gait disturbance is one of the hardest to treat; pharmacological, deep brain stimulation (DBS) and physical therapies lead to only partial improvements (Nonnekes et al., 2020, 2015). While the subthalamic nucleus (STN) and globus pallidus (GPi) are common DBS targets for PD, alternative targets such as pedunculopontine nucleus (PPN) and the zona incerta (ZI) have been proposed with mixed results in improving postural and/or gait dysfunctions (Caire et al., 2013; Ferraye et al., 2010; Gut and Winn, 2015; Hamani et al., 2011; Moro et al., 2010; Nonnekes et al., 2015; Okun and Foote, 2010; Ossowska, 2019; Stefani et al., 2007; Thevathasan et al., 2018). Part of the issue with targeting the ZI with DBS strategies is the relative lack of knowledge regarding its downstream anatomical and functional connectivity with motor centres. Recent work with photoactivation of subpopulations of PPN neurons in PD models shows promise for similar ZI-focused strategies (Masini and Kiehn, 2022).

The ZI is recognized as an integrative hub, with roles in regulating sensory inflow, arousal, motor function, and conveying motivational states (Mitrofanis, 2005; Wang et al., 2020). As such, it is well placed to be involved in PD and has seen increased clinical and preclinical research over the last two decades (Blomstedt et al., 2018; Ossowska, 2019; Plaha et al., 2008). However, little attention has been placed on the medial zona incerta (mZI), particularly the A13, the only dopamine-containing region of the rostral ZI (Bolton et al., 2015; Kim et al., 2017; Sharma et al., 2018). Recent research in primates and mice (Peoples et al., 2012; Roostalu et al., 2019; Shaw et al., 2010) indicates that the A13 is preserved in 1-methyl-4-phenyl-1,2,3,6-tetrahydropyridine (MPTP)-based PD models.

Recently, we discovered that the A13 located within the ZI projects to two areas of the mesencephalic locomotor region (MLR), the PPN and cuneiform nucleus (CnF)(Sharma et al., 2018), suggesting a role for A13 in locomotor function. Indeed, *in vivo* photometry recordings from calcium/calmodulin-dependent protein kinase IIα (CaMKIIα) populations in the rostral ZI, which includes the A13 nucleus, show a subpopulation of cells whose activity correlates with movement speed (Li et al., 2021). Since this region projects to the MLR, it is a potential parallel motor pathway to target for gait improvement. Photoactivation of glutamatergic MLR neurons alleviates motor deficits in the 6-OHDA mouse model (Fougère et al., 2021; Masini and Kiehn, 2022). Phenomena such as kinesia paradoxa (Glickstein and Stein, 1991) in PD patients support the existence of preserved parallel motor pathways that can be engaged in particular circumstances to produce normal movement.

Further evidence supporting the importance of parallel motor pathways in PD includes those reporting functional alterations in A13 (Hoffman et al., 1997; Périer et al., 2000). Nigrostriatal lesions affect A13 cellular function and lead to anatomical remodeling in monoaminergic brain regions (Braak et al., 2003; Kish et al., 2008; Lim et al., 2009; Perez-Lloret and Barrantes, 2016; Roostalu et al., 2019; Scatton et al., 1983; Zweig et al., 1989). The A13 connectome encompasses the cerebral cortex (Mitrofanis and Mikuletic, 1999), central nucleus of the amygdala (Eaton et al., 1994), thalamic paraventricular nucleus (Li et al., 2014), thalamic reuniens (Sita et al., 2007; Venkataraman et al., 2021), MLR(Sharma et al., 2018), superior colliculus (SC) (Bolton et al., 2015), and dorsolateral periaqueductal grey (PAG) (Messanvi et al., 2013; Sita et al., 2007), making the A13 an important hub for goal-directed locomotion

(Choi and McNally, 2017; Eaton et al., 1994; Messanvi et al., 2013; Mok and Mogenson, 1986; Moriya et al., 2020; Ogundele et al., 2017; Manjit K. Sanghera et al., 1991; M. K. Sanghera et al., 1991; Sita et al., 2007; Venkataraman et al., 2021).

Based on the role of the A13 in gait and, specifically, as a possible target to improve gait in PD, we investigated the therapeutic potential of photoactivating a tightly circumscribed region targeting a small region containing mainly the A13 and a small area of the mZI, which we term A13 region throughout the manuscript. We identified areas of preservation and plasticity within the mZI connectome using whole-brain imaging techniques. Photoactivation of the A13 region rescued bradykinetic and akinetic symptoms in a mouse model of 6-hydroxydopamine (6-OHDA) mediated unilateral nigrostriatal degeneration. Because the zona incerta is a hub for the rapid selection of motor function, we then mapped the input and output patterns of the region. We found evidence of a global remodeling of afferent and efferent projections of the A13 region. While endogenous compensatory mechanisms from the remaining but remodelled A13 region connectome were inadequate in overcoming locomotor deficits observed in 6-OHDA mice, photostimulation of the A13 region restored locomotor activity. These data demonstrate that the A13 region produces powerful pro-locomotor effects in normal and PD mouse models. Moreover, PD-related bradykinesia is ameliorated with A13 region photoactivation in the presence of remodelling of the A13 region connectome. Some of these data have been published in abstract form (L. Kim et al., 2021).

RESULTS

Unilateral 6-OHDA mouse model has robust motor deficits

The overall experimental design is illustrated in Figure 1A, along with a schematic in Figure 1B showing injections of 6-OHDA in the medial forebrain bundle and AAVDJ-CaMKIIα-ChR2 virus into the medial zona incerta (mZI). We confirmed substantia nigra pars compacta (SNc) degeneration in a well-validated unilateral 6-OHDA-mediated Parkinsonian mouse model (Thiele et al., 2012). The percentage of tyrosine hydroxylase (TH^+) cell loss normalized to the intra-animal contralesional side was quantified. 6-OHDA produced a significant lesion that decreased TH^+ neuronal SNc populations. As previously reported (Boix et al., 2015), the SNc ipilesional to the 6-OHDA injection (n = 10) showed major ablation of the TH^+ neurons compared to sham animals (Figure 1C and D: n = 11).

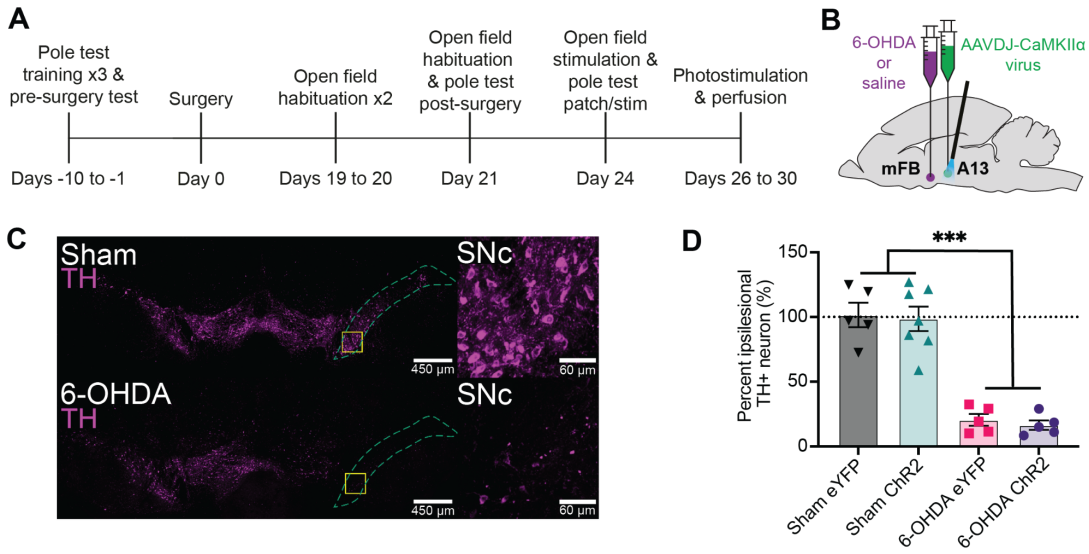

Figure 1. Experimental design and confirmation of unilateral TH$^+$ depletion in the SNc via 6-OHDA lesion. (**A**) Illustration of experimental timeline. (**B**) Dual ipsilateral stereotaxic injection into the MFB and A13 region. (**C**) TH$^+$ cells in SNc of sham (top) compared to 6-OHDA injected mouse (bottom). Magnified areas outlined by yellow squares are shown on the right. (**D**) Unilateral injection of 6-OHDA (6-OHDA ChR2: $n = 5$, 6-OHDA eYFP: $n = 5$) into the MFB resulted in greater percentage of TH$^+$ loss compared to sham in the SNc (sham ChR2: $n = 7$, sham eYFP: $n = 5$, three-way MM ANOVAs), regardless of virus type ($F_{1,18} = 104.4$, $p < .001$). ***$p < .001$. Error bars indicate SEMs.

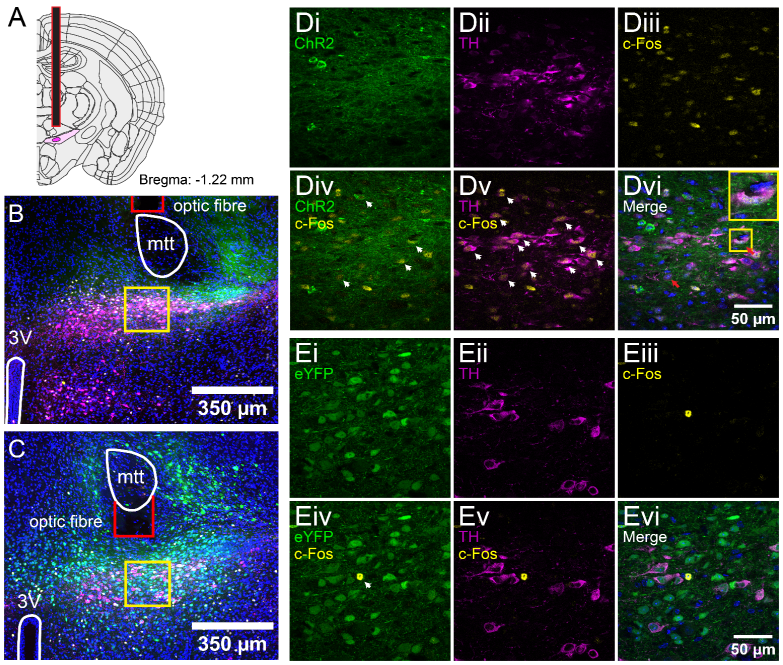

Figure 2. *Post hoc* c-Fos expression and targeting of the mZI and A13. **(A)** Diagram showing the A13 DAergic nucleus in dark magenta encapsulated by the ZI in light magenta. The fibre optic tip is outlined in red. Atlas image adapted from the Allen Brain Atlas (Goldowitz, 2010). **(B)** Tissue images were obtained from 6-OHDA ChR2 animals around bregma -1.22 mm, and **(C)** a 6-OHDA eYFP animal more caudally around bregma -1.46 mm. Images show the distribution of DAPI (blue), eYFP (green), c-Fos (yellow), and TH (magenta). Landmarks are outlined in white (3V: third ventricle; mtt: mammillothalamic tract), and the optic cannula tip is shown in red. Higher magnification images of the A13 DAergic nucleus are outlined by the yellow boxes in a 6-OHDA ChR2 animal **(D)** and a 6-OHDA eYFP animal **(E)**. Scale bars are set to 350 µm. Images show isolated channels in the top rows of the respective groups: eYFP **(i)**, TH **(ii)**, and c-Fos **(iii)**. Merged channels for eYFP and c-Fos **(iv)**, TH and c-Fos **(v)**, and a merge of all four channels **(vi)** are presented in the bottom rows of their respective groups. White arrowheads in the merged images highlight overlap in merged markers. Red arrows show triple colocalization of eYFP, c-Fos and TH. **(Dvi)** contains a magnified example of triple-labelled neurons, as highlighted in the yellow box. Scale bars are set to 50 µm.

A13 region photoactivation generates pro-locomotor behaviors in the open field

6-OHDA lesions are characterized as generating bradykinetic and akinetic phenotypes in the open field (Li et al., 2022; Magno et al., 2019; Masini and Kiehn, 2022; Sanders and Jaeger, 2016). To understand the impact of A13 region photoactivation on locomotion in sham and PD model mice, on-target localization of ferrule above the A13 region, centered on the mZI, along with YFP reporter expression, was confirmed (Figure 2) in mice given sham or 6-OHDA injections. Corroborating the *post hoc* targeting, we found evidence for c-Fos in neurons within the A13 region in photostimulated ChR2 mice (Figure 2). Before *post hoc* analysis, mice were monitored in the open field test (OFT), where the effects of the 6-OHDA lesion were apparent, with 6-OHDA lesioned animals demonstrating far less movement, fewer bouts of locomotion, and less time engaging in locomotion in the OFT (Figure 2A-E). Notably, photoactivation of the A13 region often generated dramatic effects, with mice showing a distinct increase in locomotor behavior (Figure 3A, Movie S1 & Movie S2). Both sham and 6-OHDA ChR2 mice showed a significant increase in locomotor distance travelled during periods of photoactivation (Figure 3B, p = 0.005). One sham animal showed grooming behavior on stimulation and was excluded from the analysis.

We tested whether photoactivation led to a single bout of locomotion or if there was an overall increase in bouts, signifying that animals could repeatedly initiate locomotion following photoactivation. Mice in the ChR2 groups demonstrated an increase in the number of locomotion bouts with photoactivation, indicating a greater ability to start locomotion from rest, and that photoactivation was not eliciting a single prolonged bout (Figure 3C, p = 0.005). When we examined each bout of locomotion, photoactivation increased the total duration of locomotion (Figure 3D, p = 0.005). There was a refractory decrease in the distance travelled by the sham ChR2 animal group (Figure S1A), which was not evident for the 6-OHDA cohort (Figure S1B). To control for this, we compared the pre-timepoints to the baseline one-minute averages to ensure that the animal locomotion distance travelled returned to a stable state before stimulation was reapplied (Figure S1C, p = 0.783).

Next, we examined the reliability of photoactivation to initiate locomotion. The percentage of trials with at least one bout of locomotion was compared for the pre-and stim time points. 6-OHDA ChR2 animals showed a reliable pro-locomotion phenotype with A13 region photoactivation (Figure S2A: p = 0.042). As was expected in the control 6-OHDA eYFP group, there was no effect of photoactivation on the probability of engaging in locomotion (p = 0.713).

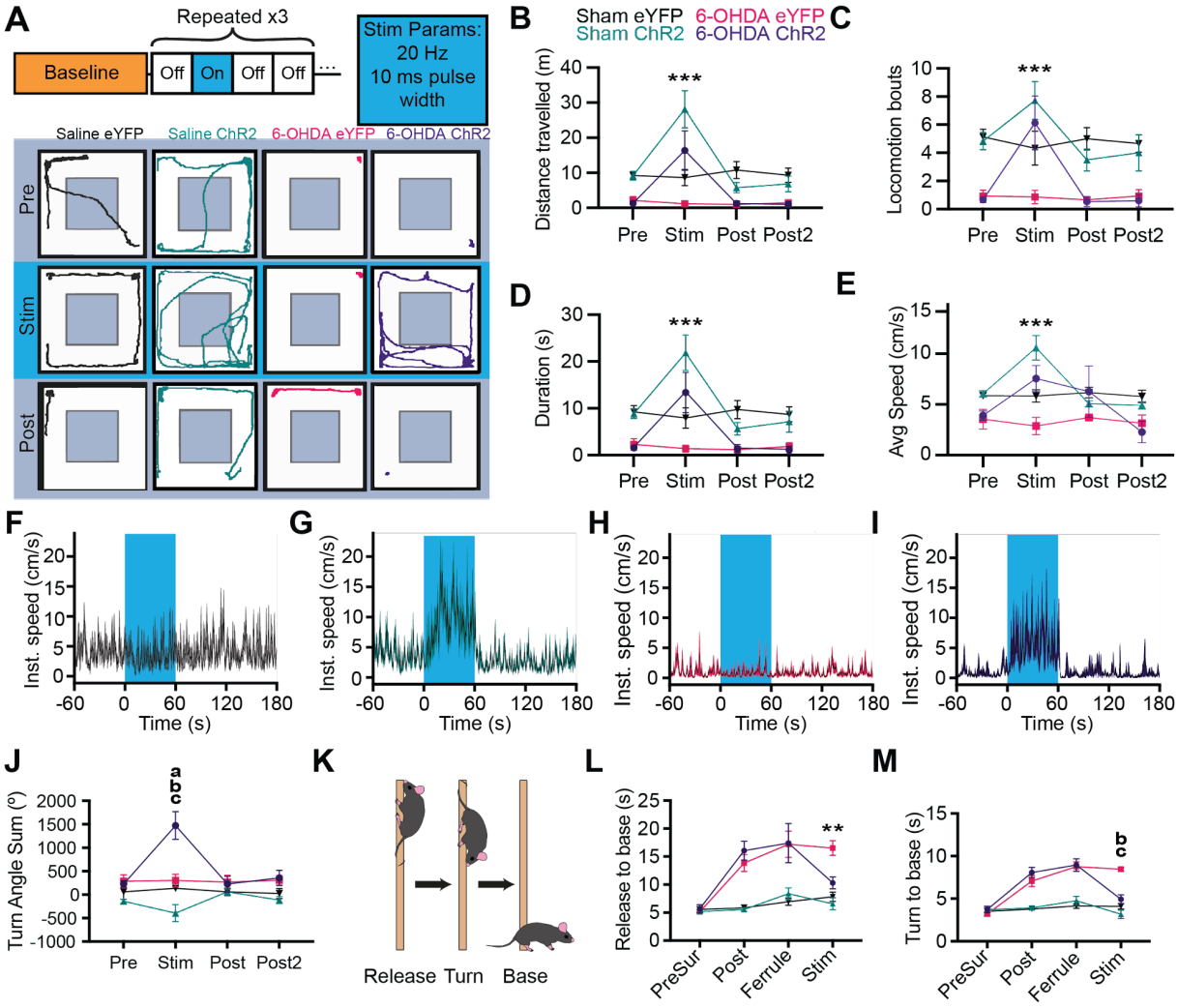

Figure 3. Ipsilesional photoactivation of the A13 region in a unilateral 6-OHDA mouse model rescues motor deficits.

(**A**) Schematic of open field experiment design and example traces for open field testing (1 min) with unilateral photoactivation of the A13 region. (**B-E**) Effects of photoactivation on open field metrics for sham eYFP (n = 5), sham ChR2 (n = 6), 6-OHDA eYFP (n = 5), and 6-OHDA ChR2 (n = 5) groups (three-way MM ANOVAs, *post hoc* Bonferroni pairwise). Photoactivation increased in the ChR2 groups: (**B**) distance travelled (ChR2 vs. eYFP: p = 0.005), (**C**) locomotor bouts (ChR2 vs. eYFP: p = 0.005), (**D**) duration of locomotion in the open field (ChR2 vs. eYFP: p = 0.005), and (**E**) animal movement speed (ChR2 vs. eYFP: $p < 0.001$). (**F-I**) Group averaged instantaneous velocity graphs showing no increase in a sham eYFP (**F**) or 6-OHDA eYFP mouse (**H**), with increases in velocity during stimulation in a sham ChR2 (**G**) and 6-OHDA ChR2 (**I**) mouse. (**J**) The graph presents animal rotational bias using the turn angle sum. There was a significant increase in 6-OHDA ChR2 rotational bias during A13 region photoactivation (6-OHDA ChR2 vs. 6-OHDA eYFP: $p < 0.001$). (**K**) Diagram depicting the pole test. A mouse is placed on a vertical pole facing upwards. The time for release is taken as the experimenter removes their hand from the animal's tail. (**L, M**) Graphs showing the response of animals to photoactivation of the A13 region while performing the pole test. (**L**) A13 region photoactivation also led to shorter total descent time in ChR2 compared to eYFP mice (ChR2 vs. eYFP: p = 0.004), and (**M**) 6-OHDA ChR2 mice showed a greater reduction in descent time compared to sham ChR2 (6-OHDA ChR2 vs. sham ChR2: p = 0.012; 6-OHDA ChR2: n = 5; sham ChR2: n = 7). ***$p < .001$, **$p < .01$, *$p < .05$. Bonferroni's *post hoc* comparisons between 6-OHDA ChR2 and sham eYFP, sham ChR2, and 6-OHDA eYFP at stim time point as a, b, and c respectively. Error bars indicate SEMs.

Animal movement speed also factors into the total distance travelled measure and can be discussed in regard to a bradykinetic phenotype in 6-OHDA lesioned mice (Magno et al., 2019; Masini and Kiehn, 2022; Sanders and Jaeger, 2016). Using instantaneous animal movement speeds that exceeded 2 cm/s as per Masini & Kiehn (2022), we plotted instantaneous speed (Figure 3F-I) and analyzed one-minute bins (Figure 3E). As was expected, 6-OHDA lesioned animals had lower movement speeds than sham control animals ($p < 0.001$). One animal from the 6-OHDA eYFP group was excluded because it did not meet the speed threshold during recording. Both the 6-OHDA ChR2 and sham ChR2 groups displayed increases in average speed during photostimulation (Figure 3E, $p < 0.001$). When we examined the time taken to initiate locomotion, there was no significant difference between sham or 6-OHDA ChR2 groups (Figure S2B).

Photoactivation of the A13 region increases ipsilesional turning in the open field test

Unilateral 6-OHDA lesions drive asymmetric rotational bias (Boix et al., 2015; Li et al., 2022; Magno et al., 2019; Thiele et al., 2012). We were interested in whether this persisted with stimulation and noted upon observation of photoactivation that animals appeared to have increased ipsilesional rotation. As observed, 6-OHDA ChR2 animals had an increase in turn angle sum (TAS), indicating an increase in their rotational bias with photoactivation in the ipsilesional direction (Figure 3J, $p < 0.001$). As expected, 6-OHDA eYFP animals showed consistent rotational bias throughout time. The rotational bias of sham ChR2 was also compared to determine whether the increased rotational bias was due to photoactivation or the interaction of photoactivation and the lesion. The sham ChR2 group showed no significant change in TAS with photoactivation (Figure 3J, $p > 0.05$). Next, we examined whether the increased turning angle sum in the 6-OHDA ChR2 group was observed during periods of locomotion. When the TAS was calculated only during periods of locomotion, the rotational bias in the animal orientation in the 6-OHDA ChR2 animals was not observed ($p = 0.286$).

Skilled vertical locomotion is improved in the pole test with photoactivation of the A13 region.

The pole test is a classic 6-OHDA behavioral paradigm (Figure 3K) that involves skilled locomotor abilities for an animal to turn and descend a vertical pole (Matsuura et al., 1997; Ogawa et al., 1985). Improvements in function can be inferred if the time taken to complete the test decreases (Matsuura et al., 1997; Ogawa et al., 1985). 6-OHDA mice demonstrated significantly greater descent times than sham mice ($p < 0.001$). Photoactivation of the A13 region reduced descent times for both 6-OHDA and sham groups on the pole test (Figure 3L, $p = 0.004$, Movie S3). Neither of the eYFP groups showed any changes in the time to complete the pole test.

To further understand the effects of photoactivation on the ability of mice to descend the pole, the time taken for mice to descend after turning was analyzed to remove any influence of animals spending time investigating their environment on the top of the pole. While all groups showed reduced total pole test descent time with photoactivation, considering just the time to descend from turn alone, there was a larger improvement with A13 region photoactivation in the 6-OHDA ChR2 mice compared to sham ChR2 mice (Figure 3M: $p = 0.012$). These results indicate that photoactivation has the effect of reducing bradykinesia by improving the ability of mice to descend the pole during the PT.

Dopaminergic Cells in the A13 region are preserved in the unilateral 6-OHDA mouse model

While photoactivation of the A13 region promoted locomotor activity in both sham and 6-OHDA mice, there were differences in speed and directional bias. We hypothesized that this may be due to changes in the A13 region connectome since there is evidence of changes in firing and metabolic activity in the region (Périer et al., 2000). Therefore, we utilized whole brain imaging approaches (Hansen et al., 2020; Zhan et al., 2021) to examine changes in the connectome following 6-OHDA lesions of the nigrostriatal region.

Using whole brain imaging, as expected, TH^+ cells in SNc were more vulnerable to the 6-OHDA neurotoxin than the ventral tegmental area (VTA) and A13 (Figure S3A-F). 6-OHDA- treated mice showed a significantly greater percentage of TH^+ cell loss in SNc compared to the VTA and A13 (VTA vs. SNc: $p = 0.003$; A13 vs. SNc: $p = 0.005$). In contrast, sham animals showed no significant difference in TH^+ cell loss across SNc, VTA and A13 (Figure S3G, $p > 0.05$). Thus, similar to that observed in the human brain of Parkinsonian patients (Matzuk and Saper, 1985), there is a remarkable preservation of dopaminergic cells in the A13 after nigrostriatal degeneration in the 6-OHDA mouse model of PD.

Large-scale changes in the A13 region connectome following 6-OHDA-mediated unilateral nigrostriatal degeneration

Although photoactivation had benefits in restoring speed in 6-OHDA mice (Figure 3), circling behavior was increased, suggesting additional changes that may reflect connectome alterations. We examined the changes in the input and output of the A13 by co-injecting anterograde (AAV8-CamKII-mCherry) and retrograde AAV (AAVrg-CAG-GFP) tracers into the A13 nucleus (Keith B. J. Franklin and Paxinos, 2008). The injection core and spread were determined in the rostrocaudal direction from the injection site (Figure S4). To examine whether unilateral nigrostriatal degeneration resulted in changes in the organization of inputs and outputs from the A13, we first visualized interregional correlations of afferent and efferent proportions for each condition using correlation matrices (Fig 4A and B; 251 regions in a pairwise manner). Correlation matrices were organized using the hierarchical anatomical groups from the Allen Brain Atlas (Figure 4C). To minimize the influence of experimental variation on the total labeling of neurons and fibers, the afferent cell counts or efferent fiber areas in each brain region were divided by the total number found in a brain to obtain the proportion of total inputs and outputs. The data were normalized to a $\log_{10}$ value to reduce variability and bring brain regions with high and low proportions of cells and fibers to a similar scale (Kimbrough et al., 2020). Comparing the afferent and efferent proportions in a pairwise manner between mice showed good consistency with an average correlation of 0.91 ± 0.02 (Spearman's correlation, Figure S5).

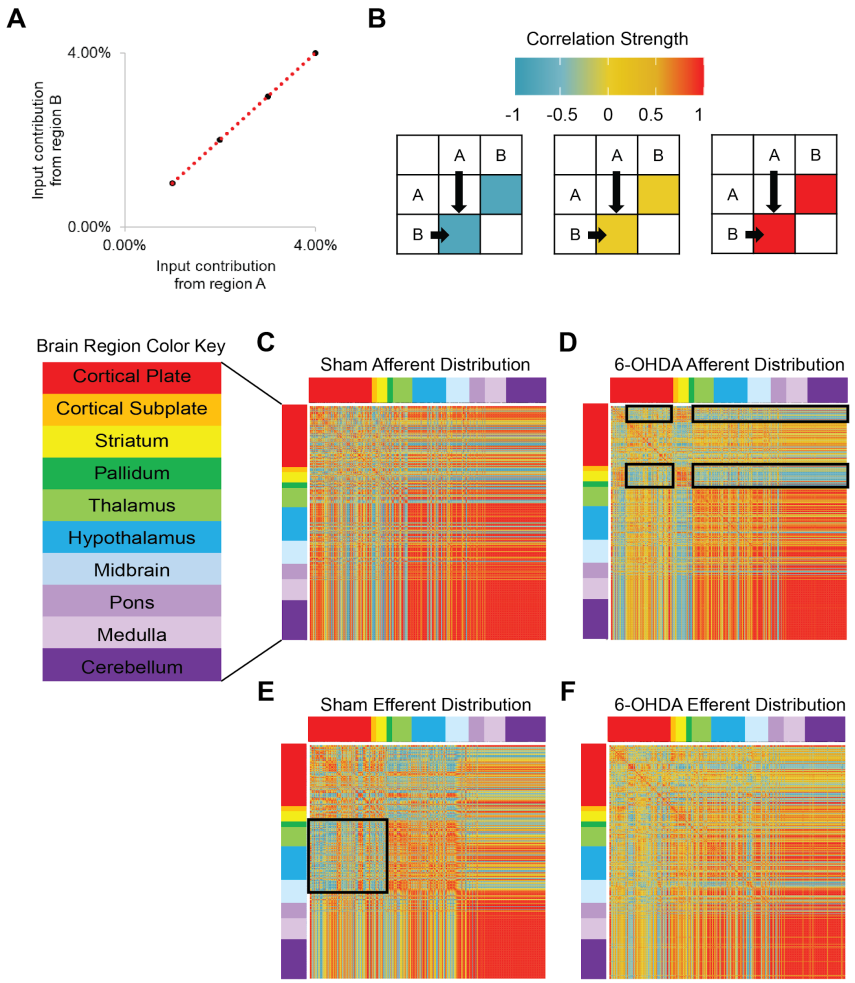

Figure 4. Unilateral nigrostriatal degeneration leads to large-scale changes in the organization of the A13 region afferent and efferent distributions across the neuraxis.
We used correlation matrices to summarize any observable patterns in the distribution patterns of inputs and outputs of the A13 region. A correlation matrix was calculated by correlating the proportion of input from one brain region to another in a pairwise manner across 251 brain regions delimited by registration with Allen Brain Atlas. If two brain regions among mice (eg. brain regions A and B) contribute a similar input, they are highly correlated **(A)**. Using the color legend showing various correlation strengths, the intersecting box in the matrix in this example will be colored dark red **(B)**. If no relationship is found between contributions from two brain regions, the intersecting box will be colored yellow. If the contribution from one brain region was negatively correlated with another brain region among mice, then the intersecting box will be colored blue. The afferent distribution pattern in the sham displayed a higher level of inter-regional correlation between brain regions **(C)** than 6-OHDA injected mice **(D)**. Indeed, two distinct bands of anti-correlated afferent regions were identified in the 6-OHDA injected mice (see black boxes in **D**). These two bands arose from the cortical plate subregions (motor, sensory, visual, and prefrontal), and striatal and pallidal subregions showing distinct inputs compared to the rest of the neuraxis. In contrast, the projection patterns of A13 efferents displayed a higher level of inter-regional correlation between brain regions following a unilateral nigrostriatal degeneration **(F)** compared to sham **(E)**. In sham, proportions of A13-cortical/ striatal efferents were negatively correlated to A13-pallidal/ thalamic/ hypothalamic/ midbrain efferents (see black boxes in **E**). However, these distinct projection patterns disappeared following nigrostriatal degeneration, suggesting A13 efferent distributions becoming more distributed across the neuraxis.

We observed changes in projection patterns between the sham and the 6-OHDA group. A correlation matrix was used to quantify the relationship of input from brain regions in a pairwise manner through the neuraxis. Overall, afferents onto the A13 in sham animals displayed a higher interregional correlation between brain regions than 6-OHDA-injected mice. Specifically, correlation coefficients of 0.10, 0.30, and 0.50 or larger represent weak, moderate, and strong correlations, respectively (Cohen, 1988). Compared to sham (Figure 4C), in 6-OHDA injected mice (Figure 4D), afferent contributions from two clusters of brain subregions became more dissimilar (anti-correlated) to the rest of the neuraxis: 1) cortical plate subregions (motor, sensory, visual, and prefrontal), and 2) striatal, and pallidal subregions compared to sham (boxed blue areas in Figure 4D). These data suggest that afferents from several regions showed a coordinated reduction in afferent density onto the A13, except contributions from cortical plate (motor, sensory, visual, and prefrontal), striatal, and pallidal subregions that were positively correlated. In other words, contributions from the cortical plate (motor, sensory, visual, and prefrontal), striatal and pallidal subregions are positively correlated, but compared to the rest of the brain, they are anti-correlated. This suggests a greater afferent input onto A13 from the cortical plate (motor, sensory, visual, and prefrontal), striatal and pallidal subregions than other regions after 6-OHDA lesions.

In marked contrast, the projection patterns of A13 efferents exhibited a higher level of interregional correlation between brain regions following a unilateral nigrostriatal degeneration compared to sham. In the sham condition, the A13 connectome is biased towards cortical and striatal regions compared to pallidal, thalamic, hypothalamic, midbrain efferents. This is shown by a broad negative correlation between these two large groups (Figure 4E). However, these broad anti-correlations disappear following nigrostriatal degeneration (Figure 4F). These data indicate that the A13 efferent connectome is less refined following nigrostriatal degeneration.

Differential remodeling of A13 region connectome ipsi- and contra-lesion following 6-OHDA-mediated nigrostriatal degeneration

The distributions of the A13 connectome in sham animals served as the basis for an in-depth comparison of the preservation and plasticity of A13 afferents and efferents in 6-OHDA mouse models (Figure 5). We observed a global remodeling of A13 afferents and efferents following unilateral nigrostriatal degeneration (Figure 5A, B; E, F) that was differentially expressed across the neuraxis (Figure 4D, H). The ipsilesional side showed more downregulated areas (Figure 5D: see also example traces). These downregulated areas were focused within the cortical plate and cortical subplate regions. 6-OHDA injections also downregulated A13 afferent densities from the striatum, pallidum, thalamus and medulla. While 6-OHDA mainly downregulated ipsilesional A13 afferent densities, the hypothalamus (including ZI), midbrain, pons, and cerebellum had increased A13 afferent densities.

The intact, contralesional side showed more upregulated regions across the neuraxis, suggesting compensatory upregulation in the unilateral 6-OHDA model (Figure 5D). The cortical plate, striatum, and cortical subplate were the top three upregulated contralesional regions. In contrast, contralesional A13 afferent densities from the pallidum and thalamus were spared and upregulated. Thus, compensatory upregulation of A13 afferent density from these regions appeared lateralized from the intact, contralesional side. Furthermore, bilateral compensatory upregulation of A13 afferents was observed from the hypothalamus (including ZI), midbrain and pons.

The A13 efferents were more downregulated on the ipsilesional side (Figure 5H). However, the downregulation was focused within the isocortical, striatal and cortical subplate regions. Remodeling on the contralesional efferent projection patterns closely followed the changes seen with the afferents, except for projections onto the thalamic and midbrain regions. The A13 efferents onto thalamic regions were bilaterally upregulated. Also, the A13-midbrain efferents were upregulated ipsilesionally.

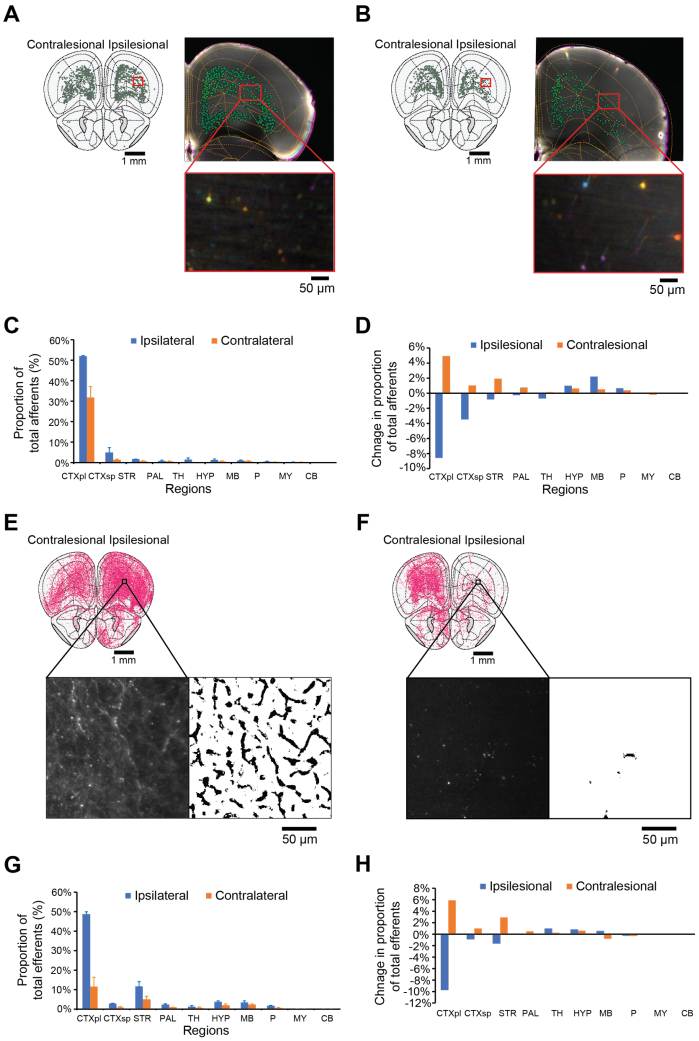

Figure 5. Differential remodeling of A13 region connectome following a unilateral nigrostriatal degeneration.
The distributions of the A13 connectome in sham served as a basis for an in-depth comparison against 6-OHDA mouse models. Example registered slices (using WholeBrain software 64 with light-sheet data, 2X objective, 4X optical zoom) at rostral areas show changes in sham **(A)** afferents compared to 6-OHDA lesioned animals **(B)**. Graph showing major brain regions contributing afferents to A13 in sham mice **(C)**. The graph illustrates the change in the proportion of afferents in 6-OHDA compared to sham mice **(D)**. Representative registered slices showing sham proportions of efferents in sham **(E)** compared to 6-OHDA mice **(F)**. The magnified black box section displays an example of mCherry+ fibers (left) segmented using Ilastik and ImageJ software (right). Graph showing major brain regions receiving efferents from the A13 in sham mice **(G)**. The graph illustrates the change in the proportion of efferents in 6-OHDA compared to sham mice **(H)**. Error bars represent SEMs. Anterograde and retrograde viruses were injected into the ipsilesional A13 (see methods). Abbreviations from Allen Brain. Atlas: CTXpl (cortical plate), CTXsp (cortical subplate), STR (striatum), PAL (palladium), TH (thalamus), HYP (hypothalamus), P (pons), MB (midbrain), MY (Medulla), and CB (cerebellum).

DISCUSSION

Our work demonstrates robust pro-locomotor effects induced by photoactivation of the A13 region in lesioned and sham mice. Photoactivation during the OFT increased locomotion distance travelled, the duration of locomotion, and speed in both sham and 6-OHDA mice. Uniquely, the 6-OHDA group had increases in the number of locomotor bouts which resembled the normal number of bouts observed in healthy mice at baseline. Bradykinesia in 6-OHDA mice was substantially improved following photoactivation. We found extensive input and output connectivity of the A13, which was remodeled following nigrostriatal lesions. Afferent input patterns displayed a marked reduction in interregional correlation across brain regions in 6-OHDA mice, while efferent projections increased. This demonstrates

the impact of nigrostriatal lesions on dopaminergic-containing regions outside the nigrostriatal zone. These findings highlight the pro-locomotory effect, therapeutic potential, and plasticity of the A13.

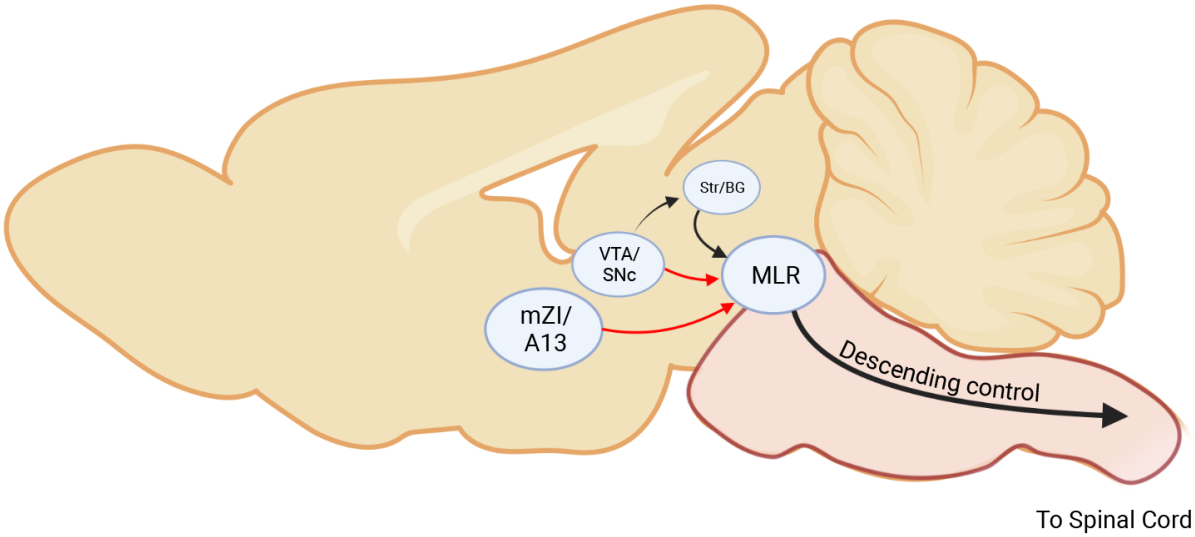

Figure 6: Comparing descending dopamine pathways for locomotor control. Simplified connectivity map for the 3 dopamine pathways. The first pathway is the classical VTA/SNc projection to the striatum, and the SNr/GPi projects to the MLR. The VTA/SNc also directly projects to the MLR (Ryczko et al., 2016). The mZI/A13 region projects dopaminergic projections to the MLR (Sharma et al., 2018). Canonical pathways are in black, while non-canonical pathways are in red.

The role of the A13 region in locomotion in sham mice

We provide the first direct evidence of the photoactivation of the A13 being sufficient in driving locomotion. It is now evident that the pro-locomotor function of ZI extends further rostrally than previous work in caudal ZI (cZI) indicates (Mitrofanis, 2005): photoactivation of cZI neurons increased animal movement speed in prey capture (Zhao et al., 2019) and active avoidance (Hormigo et al., 2020). Previous data targeting the mZI region, including somatostatin (SOM^+), calretinin (CR^+), and $vGlut2^+$ neurons, did not change locomotor distance travelled in the OFT (Li et al., 2021). In our work, there may be a combinatorial effect of multiple populations being photostimulated or targeting more medial populations in the ZI. Our results are consistent with *in vivo* calcium dynamics from $CaMKII\alpha^+$ rostral ZI cells, which overlap the A13 showing subpopulations whose activity correlates with either movement speed or anxiety-related locations (Li et al., 2021). Enhancement of the A13 activity appears to modulate locomotor activity in naive mice differently from more lateral GABAergic ZI populations (dorsal and ventral ZI). Microinjection of $GABA_A$ receptor agonists, muscimol (Wardas et al., 1988) or etomidate (Chen et al., 2023), into the ZI either evokes severe catalepsy or a significant reduction in locomotor distance and velocity, respectively. Suppression of GABAergic ZI activity can either increase locomotion

by microinjection of $GABA_A$ receptor antagonist bicuculline (Périer et al., 2002) or induce bradykinesia and akinesia by chemogenetic or optogenetic inhibitions in healthy naive mice (Chen et al., 2023).

Furthermore, our previous work showing A13 projections to the MLR is consistent with our observed photoactivation effects. We, and others, demonstrated that the A13 contains DA neurons, which may contribute to the observed effects, possibly via $D_{1/5}$ receptor activation (Ryczko et al., 2016). A13 region photoactivation produces increased locomotor speed averaging 13 cm/s and improves descent times on the pole test. The enhanced ability to perform the pole test, which requires the animal to grasp the vertical pole to descend safely without falling, provides further evidence for the role of A13 region neurons in movements. Since A13 stimulation did not alter coordination during the task, it suggests a complex behavioral role consistent with its upstream location from the brainstem and extensive connectome. A13 photoactivation increases animal speed, duration, and distance travelled. Interestingly, the latency in A13 to observe increases in ongoing animal speed or to initiate locomotion is long in both 6-OHDA and sham mice (~ 15 and 5 seconds, respectively). Second-long delays are often typical of sites upstream of the cuneiform, such as the dlPAG, which has a delay of several seconds (Tsang et al., 2021). The delays in locomotor initiation and context-specific integration following stimulation of upstream CnF targets may offer a therapeutic advantage for overcoming gait dysfunction.

Photoactivation of the A13 reduces bradykinesia and akinesia in mouse PD models

Several studies have focused on the basal ganglia by targeting the subthalamic nucleus (Gradinaru et al., 2009; Yoon et al., 2014), endopeduncular nucleus (Moon et al., 2018; Yoon et al., 2020), SNc (Kravitz et al., 2010), striatum (Bordia et al., 2016; Ryan et al., 2018), cZI (Li et al., 2022), and motor cortex (Magno et al., 2019; Sanders and Jaeger, 2016; Valverde et al., 2020), or their projections in mouse models of PD. MLR subpopulations have been explored as a target for PD DBS with mixed results (Fougère et al., 2021; Masini and Kiehn, 2022). Recently, Li et al. found that cZI glutamatergic neurons were overactive after administering 6-OHDA into the striatum, and photoinhibition rescued the motor deficits (Li et al., 2022). Motor deficits in a 6-OHDA-induced PD mouse model were also ameliorated by chemogenetic and optogenetic activation of dorsal and ventral ZI GABAergic neurons (Chen et al., 2023). Here, we introduce a novel subpopulation in ZI (A13 cells) whose photoactivation rescued bradykinetic and akinetic deficits observed in the 6-OHDA mice.

Our work shows that A13 projections are affected at cortical and striatal levels following 6-OHDA, consistent with our observed changes in locomotor function. Over 28 days, there was a remarkable change in the afferent and efferent A13 regional connectome, despite the preservation of TH^+ ZI cells. This is consistent with previous reports of widespread connectivity of the ZI (Mitrofanis, 2005). The preservation of A13 is expected since A13 lacks DAT expression (Bolton et al., 2015; Negishi et al., 2020; Sharma et al., 2018) and is spared from DAT-mediated toxicity of 6-OHDA (Dauer and Przedborski, 2003; Konnova et al., 2018; Simola et al., 2007). While A13 cells are spared following nigrostriatal degeneration, our work demonstrates its connectome is rewired. The ipsilateral afferent projections were markedly downregulated, while contralesional projecting afferents showed upregulation. In contrast, efferent projections showed less downregulation in the cortical subplate regions and bilateral upregulation of thalamic and hypothalamic efferents. Similar timeframes for anatomical and functional plasticity affecting neurons and astrocytes following an SNc or MFB 6-OHDA have been previously reported (Bosson et al., 2015; Perović et al., 2005; Requejo et al., 2020). Human PD brains that show degeneration of the SNc

have a preserved A13 region, suggesting that our model, from this perspective, is externally valid (Matzuk and Saper, 1985).

Combined with photoactivation of the A13 region, we provide evidence for plasticity following damage to SNc. A previous brain-wide quantification of TH levels in the MPTP mouse model identified additional complexity in regulating central TH expression compared to conventional histological studies (Roostalu et al., 2019). Roostalu et al. reported decreased SNc TH^+ cell numbers without a significant change in TH^+ intensity in SNc and increased TH^+ intensity in limbic regions such as the amygdala and hypothalamus (Roostalu et al., 2019). Likewise, we found no significant change in A13 TH^+ cell counts. Still, there was a downstream shift in the distribution pattern of A13 efferents following nigrostriatal degeneration with a pullback on outputs to cortical and striatal subregions. This suggests A13 efferents are more distributed across the neuraxis than in sham mice. The preserved A13 efferents could provide compensatory dopaminergic innervation with collateralization mediated contralesionally and, in some subregions, ipsilesionally to increase the availability of extracellular dopamine. Considering A13-MLR efferents (Sharma et al., 2018) that remain preserved, photoactivation of glutamatergic MLR neurons alleviates motor deficits in the 6-OHDA mouse model (Fougère et al., 2021; Masini and Kiehn, 2022), and photoactivation of A13 somata promotes locomotion in 6-OHDA mice - hypotheses that warrant further investigation.

Several A13 efferent targets could be responsible for rotational asymmetry. In a unilateral 6-OHDA model, ipsiversive circling behaviour is indicative of intact striatal function on the contralesional side (Carey, 1991; Schwarting et al., 1991; Ungerstedt, 1971; Zetterström et al., 1986). Instead, the predictive value of a treatment is determined by contraversive circling mediated by increased dopamine receptor sensitivity on the ipsilesional striatal terminals (Costall et al., 1976; Lane et al., 2006). Thus, our data suggest that photoactivation of ipsilesional A13 has an overall additive effect on ipsiversive circling and represents a gain of function on the intact side that contributes to the magnitude of overall motor asymmetry against the lesioned side. Since A13 cells are preserved in PD, future therapies could use bilateral stimulations optimized for each side to minimize the overall motor asymmetry while ameliorating bradykinesia and akinesia.

With the induction of a 6-OHDA lesion, there is a change in the A13 connectome, characterized by a reduction in bidirectional connectivity with ipsilesional cortical regions. In rodent models, the motor cortices, including the M1 and M2 regions, can shape rotational asymmetry (Gradinaru et al., 2009; Magno et al., 2019; Sanders and Jaeger, 2016; Valverde et al., 2020). Activation of M1 glutamatergic neurons increases the rotational bias (Valverde et al., 2020), while M2 neuronal stimulation promotes contraversive rotations (Magno et al., 2019). Our data suggest that A13 photoactivation may have resulted in the inhibition of glutamatergic neurons in the contralesional M1. An alternative possibility is the activation of the contralesional M2 glutamatergic neurons, which would be expected to induce increased ipsilesional rotations (Magno et al., 2019). The ZI could generate rotational bias by A13 modulation of cZI glutamatergic neurons via incerto-incertal fibres (Ossowska, 2019; Power and Mitrofanis, 1999), which promotes asymmetries by activating the SNr (Li et al., 2022). The incerto-incertal interconnectivity has not been well studied, but the ZI has a large degree of interconnectivity (Sharma et al., 2018; Tsang et al., 2021) along all axes and between hemispheres (Power and Mitrofanis, 1999). However, this may only contribute minimally given that unilateral photoactivation of the A13 cells in sham mice failed to produce

ipsiversive turning behavior while unilateral photoactivation of cZI glutamatergic neurons in sham animals was sufficient in generating ipsiversive turning behavior (Li et al., 2022). Another possibility involves the A13 region projections to the MLR. With the unknown downstream effects of A13 photoactivation, there may be modulation of the PPN neurons responsible for this turning behavior (Masini and Kiehn, 2022). The thigmotaxic behaviors suggest some effects may be mediated through dlPAG and CnF (Tsang et al., 2021), and recent work suggests the CnF as a possible therapeutic target (Fougère et al., 2021; Noga and Whelan, 2022). Since PD is a heterogeneous disease, our data provide another therapeutic target providing context-dependent relief from symptoms. This is important since PD severity, symptoms, and progression are patient-specific.

Towards a preclinical model

To facilitate future translational work applying DBS to this region, we targeted the A13 region using AAV8-CamKII-mCherry viruses. The CaMKIIα promoter virus is beneficial because it is biased towards excitatory cells (Haery et al., 2019), narrowing the diversity of transfected A13 region neurons and in our hands, the viral spread was contained within the A13 region. Optogenetic strategies have been used to activate retinal cells in humans, partially restoring visual function and providing optimism that AAV-based viral strategies can be adapted in other human brain regions (Sahel et al., 2021). A more likely possibility for stimulation of deep nuclei is that DREADD technology could be adapted, which would not require any implants, but this remains a longer-term possibility. In the short-term, our work suggests that the A13 is a possible target for DBS. Gait dysfunction in PD is particularly difficult to treat, and indeed when DBS of subthalamic nucleus is deployed, a mixture of unilateral and bilateral approaches have been used (Lizarraga et al., 2016), along with stimulation of multiple targets (Stefani et al., 2007). This represents the heterogeneity of PD and underlines the need for considering multiple targets. In this regard, the identification of non-canonical dopaminergic pathways for the direct control of locomotion is promising (Figure 6). Our work highlights the A13 as a possible target, likely used in context and in concert with the activation of other identified targets.

Limitations

Currently, few PD animal models are available that adequately model the progression and the extent of SNc cellular degeneration while meeting the face validity of motor deficits (Dauer and Przedborski, 2003; Konnova et al., 2018). While the 6-OHDA models fail to capture the age-dependent chronic degeneration observed in PD, it provides additional advantages in providing robust motor deficits with acute degeneration and identifying compensatory changes compared to the unlesioned side. Moreover, it resembles the unilateral onset (Hughes et al., 1992) and persistent asymmetry (Lee et al., 1995) of motor dysfunction in PD. Another option could be the MPTP mouse model, which offers the ease of systemic administration and translational value to primate models; however, the motor deficits are variable and lack the asymmetry observed in human patients (Hughes et al., 1992; Jagmag et al., 2015; Lee et al., 1995; Meredith and Rademacher, 2011). Despite these limitations, the neurotoxin-based mouse models, such as MPTP and 6-OHDA, offer greater SNc cell loss than genetic-based models; in the case of the 6-OHDA model, it captures many aspects of motor dysfunctions in PD (Dauer and Przedborski, 2003; Jagmag et al., 2015; Konnova et al., 2018; Simola et al., 2007).

Conclusions

Parkinson's disease involves areas outside the classic nigrostriatal axis. Our work demonstrates that the A13 region drives locomotor activity and rescues bradykinetic and akinetic deficits caused by dysfunctional DAergic transmission in the basal ganglia. We show that A13 region-evoked locomotion has therapeutic potential for improving gait in advanced PD. Widespread remodelling of the A13 region connectome is critical to our understanding of the effects of dopamine loss in PD models. In summary, our findings support an exciting role for the A13 region in locomotion with demonstrated benefits in a mouse PD model and contribute to our understanding of heterogeneity in PD.

MATERIALS AND METHODS

Animals

All care and experimental procedures were approved by the University of Calgary Health Sciences Animal Care Committee (Protocol #AC19-0035). C57BL/6 male mice 49 - 56 days old (weight: M = 31.7 g, SEM = 2.0 g) were group-housed (≤ four per cage) on a 12-h light/dark cycle (07:00 lights on - 19:00 lights off) with ad libitum access to food and water, as well as cat's milk (Whiskas, Mars Canada Inc., Bolton, ON, Canada). Mice were randomly assigned to the groups described.

Surgical Procedures

We established a well-validated unilateral 6-OHDA mediated Parkinsonian mouse model (Thiele et al., 2012) (Figure 1, Movie S4). 30 minutes before stereotaxic microinjections, mice were intraperitoneally injected with desipramine hydrochloride (2.5 mg/ml, Sigma-Aldrich) and pargyline hydrochloride (0.5 mg/ml, Sigma-Aldrich) at 10 ml/kg (0.9% sterile saline, pH 7.4) to enhance selectivity and efficacy of 6-OHDA induced lesions (Thiele et al., 2012). All surgical procedures were performed using aseptic techniques, and mice were anesthetized using isoflurane (1 - 2%) delivered by 0.4 L/min of medical-grade oxygen (Vitalair 1072, 100% oxygen).

Mice were stabilized on a stereotaxic apparatus. Small craniotomies were made above the medial forebrain bundle (MFB) and the A13 nucleus within one randomly assigned hemisphere. Stereotaxic microinjections were performed using a glass capillary (Drummond Scientific, PA, USA; Puller Narishige, diameter 15 – 20 mm) and a Nanoject II apparatus (Drummond Scientific, PA, USA). 240 nL of 6-OHDA (3.6 µg, 15.0 mg/mL; Tocris, USA) was microinjected into the MFB (AP -1.2 mm from bregma; ML ±1.1 mm; DV -5.0 mm from the dura). Sham mice received a vehicle solution (240 nL of 0.2% ascorbic acid in 0.9% saline; Tocris, USA).

Whole Brain Experiments

For tracing purposes, a 50:50 mix of AAV8-CamKII-mCherry (Neurophotonics, Laval University, Quebec City, Canada, Lot #820, titre 2×10^{13} GC/ml) and AAVrg-CAG-GFP (Addgene, Watertown, MA, Catalogue #37825, Lot #V9234, titre ≥ 7×10^{12} vg/mL) was injected ipsilateral to 6-OHDA injections at the A13 nucleus in all mice (AP -1.22 mm from bregma; ML ±0.4 mm; DV -4.5 mm from the dura, the total volume of 110 nL at a rate of 23 nl/sec). Post-surgery care was the same for both sham and 6-OHDA injected mice. The animals were sacrificed 29 days after surgery.

Photoactivation Experiments

36.8 nL of AAVDJ-CaMKIIα-hChR2(H134R)-eYFP (UNC Stanford Viral Gene Core; Stanford, CA, US, Catalogue #AAV36; Lots #3081 and #6878, titres 1.9×10^{13} and 1.7×10^{13} GC/mL, respectively) or eYFP

control virus (AAVDJ-CaMKIIα-eYFP; Lots #2958 & #5510, titres 7.64×10^{13} and 2.88×10^{13} GC/mL, respectively) was injected into the A13's stereotaxic coordinates (Sharma et al., 2018). A mono-fibre cannula (Doric Lenses, Quebec, Canada, Catalogue #B280-2401-5, MFC_200/230-0.48_5mm_MF2.5_FLT) was implanted slowly 300 µm above the viral injection site. Metabond® Quick Adhesive Cement System (C&B, Parkell, Brentwood, NY, US) and Dentsply Repair Material (Dentsply International Inc., York, PA, USA) were used to fix the ferrule in place. Animals recovered from the viral surgery for 19 days before follow-up behavioral testing. Figure 1 illustrates the timeline of the behavioral tests.

ChR2 photoactivation

A Laserglow Technologies 473 nm laser and driver (LRS-0473-GFM-00100-05, North York, ON, Canada) were used to generate the photoactivation for experiments. The laser was triggered with TTL pulses from either an A.M.P.I. Master-8 stimulator (Jerusalem, Israel) or an Open Ephys PulsePal (Sanworks, Rochester, NY, US) set to 20 Hz with 10-ms pulse width. All fibre optic implants were tested for laser power before implantation (Thorlabs, Saint-Laurent, QC, Canada; optical power sensor (S130C) and meter (PM100D)). The Stanford Optogenetics irradiance calculator was used to estimate the laser power for stimulation ("Stanford Optogenetics Resource Center," n.d.). A 1×2 fibre-optic rotary joint (Doric Lenses, Quebec, Canada; FRJ_1x2i_FC-2FC_0.22) was used. The animals' behaviors were recorded with an overhead camera (SuperCircuits, Austin, TX, US; FRJ_1x2i_FC-2FC_0.22; 720 x 480 resolution; 30 fps). The video was processed online (Cleversys, Reston, VA; TopScan V3.0) with a TTL signal output from a National Instruments 24-line digital I/O box (NI, Austin, TX, US; USB-6501) to the Master-8 stimulator.

Behavioral Testing

Open Field Test

Each mouse was placed in a square arena measuring 70 (W) x 70 (L) x 50 (H) cm with opaque walls and recorded for 30 minutes using a vertically mounted video camera (Model PC165DNR, Supercircuits, Austin, TX, USA; 30 fps). 19 days following surgery, mice were habituated to the open field test (OFT) arena with a patch cable attached for three days in 30 minute sessions to bring animals to a common baseline of activity. On experimental days, after animals were placed in the OFT, a one-minute-on-three-minutes-off paradigm was repeated five times following an initial ten minutes baseline activity. Locomotion was registered when mice travelled a minimum distance of 10 cm at 6 cm/s for 20 frames over a 30-frame segment. When the mouse velocity dropped below 6 cm/s for 20 frames, locomotion was recorded as ending. Bouts of locomotion relate to the number of episodes where the animal met these criteria. Velocity data were obtained from the frame-by-frame results and further processed in a custom Python script to detect instantaneous speeds greater than 2 cm/s (Masini and Kiehn, 2022). All animals that had validated targeting of the A13 region were included in the OFT data presented in the results section, except for one sham ChR2 animal, which showed grooming rather than the typical locomotor phenotypes.

Pole Test

Mice were placed on a vertical wooden pole (50 cm tall and 1 cm diameter) facing upwards and then allowed to descend the pole into their home cage (Glajch et al., 2012). Animals were trained for three days and tested 2-5 days pre-surgery. Animals were acclimatized 21-22 days post-surgery under two

conditions: without a patch cable and with the patch cable attached without photoactivation. On days 24-27, experimental trials were recorded with photoactivation. Video data were recorded for a minimum of three trials (Canon, Brampton, ON, Canada; Vixia HF R52; 1920 x 1080 resolution; 60 fps). A blinded scorer recorded the times for the following events: the hand release of the animal's tail, the animal fully turning to descend the pole, and the animal reaching the base of the apparatus. Additionally, partial falls, where the animal slipped down the pole but did not reach the base, and full falls, where the animal fell to the base, were recorded separately. All validated animals were included in the quantified data, including the sham ChR2 animal that began grooming in the OFT upon photoactivation. This animal displayed proficiency in performing the PT during photoactivation. It started grooming upon completion of the task when photoactivation was on. One sham ChR2 animal was photostimulated at 1 mW since it would jump off the apparatus at higher stimulation intensities.

Immunohistochemistry

A13 and SNc region

Post hoc analysis of the tissue was performed to confirm the 6-OHDA lesion and validate the targeting of the A13 region. Following behavioral testing, animals underwent a photoactivation protocol to activate neurons below the fibre optic tip (Koblinger et al., 2018). Animals were placed in an OFT for ten minutes before receiving three minutes of photoactivation. Ten minutes later, the animals were returned to their home cage. 90 minutes post photoactivation, animals were deeply anaesthetised with isoflurane and then transcardially perfused with room temperature PBS followed by cold 4% paraformaldehyde (PFA) (Sigma-Aldrich, Catalogue #441244-1KG). The animals were decapitated, and the whole heads were incubated overnight in 4% PFA at 4°C before the fibre optic was removed and the brain removed from the skull. The brain tissue was post-fixed for another 6 - 12 hours in 4% PFA at 4°C then transferred to 30% sucrose solution for 48 - 72 hours. The tissue was embedded in VWR® Clear Frozen Section Compound (VWR International LLC, Radnor, PA, US) and sectioned coronally at 40 or 50 µm using a Leica cryostat set to -21°C (CM 1850 UV, Concord, ON, Canada). Sections from the A13 region (-0.2 to -2.0 mm past bregma) and the SNc (-2.2 to -4.0 past bregma) were collected and stored in PBS containing 0.02% (w/v) sodium azide (EM Science, Catalogue #SX0299-1, Cherry Hill, NJ, US) (Keith B. J. Franklin and Paxinos, 2008).

Immunohistochemistry staining was done on free-floating sections. The A13 sections were labelled for c-Fos, TH, and GFP (to enhance eYFP viral signal), and received a DAPI stain to identify nuclei. The SNc sections were stained with TH and DAPI (Table 1). Sections were washed in PBS (3 x 10 mins) then incubated in a blocking solution comprised of PBS containing 0.5% Triton X-100 (Sigma-Aldrich, Catalogue #X100-500ML, St. Louis, MO, US) and 5% donkey serum (EMD Millipore, Catalogue #S30-100ML, Billerica, MA, USA) for 1 hour. This was followed by overnight (for SNc sections) or 24-hour (for A13 sections) incubation in a 5% donkey serum PBS primary solution at room temperature. On day 2, the tissue was washed in PBS (3 x 10 mins) before being incubated in a PBS secondary solution containing 5% donkey serum for 2 hours (for SNc tissue) or 4 hours (for A13 tissue). The secondary was washed with a PBS solution containing 1:1000 DAPI for 10 mins, followed by a final set of PBS washes (3 x 10 mins). Tissue was mounted on Superfrost® micro slides (VWR, slides, Radnor, PA, US) with mounting media (Vectashield®, Vector Laboratories Inc., Burlingame, CA, US), covered with #1 coverslips (VWR, Radnor, PA, US) then sealed.

Whole Brain

Mice were deeply anesthetized with isoflurane and transcardially perfused with PBS, followed by 4% PFA. To prepare for whole brain imaging, brains were first extracted and postfixed overnight in 4% PFA at 4°C. The next day, a modified iDISCO method (Renier et al., 2014) was used to clear the samples and perform quadruple immunohistochemistry in whole brains. The modifications include prolonged incubation and the addition of SDS for optimal labelling. The antibodies used are listed in Table 1 and the protocol is provided in Table 2.

Image Acquisition and Analysis

Photoactivation Experiments

All tissue was initially scanned with an Olympus VS120-L100 Virtual Slide Microscope (UPlanSApo, 10x and 20x, NA = 0.4 and 0.75). Standard excitation and emission filter cube sets were used (DAPI, FITC, TRITC, Cy5), and images were acquired using an Orca Flash 4.0 sCMOS monochrome camera (Hamamatsu, Bridgewater Township, NJ, US). For c-Fos immunofluorescence, A13 sections of the tissue were imaged with a Leica SP8 FALCON (FAst Lifetime CONtrast) scanning confocal microscope equipped with a tunable laser and using a 63x objective (HC PlanApo, NA = 1.40).

SNc images were imported into Adobe Illustrator, where the SNc (Fougère et al., 2021), including the pars lateralis (SNl), was delineated using the TH immunostaining together with the medial lemniscus and cerebral peduncle as landmarks (bregma -3.09 and -3.68) (Iancu et al., 2005; Keith B. J. Franklin and Paxinos, 2008; Stott and Barker, 2014). Cell counts were obtained using a semi-automated approach using an Ilastik (v1.4.0b15) (Berg et al., 2019) trained model followed by corrections by a blinded counter (Fougère et al., 2021; Iancu et al., 2005). Targeting was confirmed on the 10x overview scans of the A13 region tissue by the presence of eYFP localized in the mZI around the A13 TH^+ nucleus, the fibre optic tip being visible near the mZI and A13 nucleus, and the presence of c-Fos positive cells in $ChR2^+$ tissue. C-Fos expression colocalization within the A13 region was performed using confocal images. The mZI & A13 region was identified with the 3rd ventricle and TH expression as markers (Keith B. J. Franklin and Paxinos, 2008).

Whole Brain Experiments

Cleared whole brain samples were imaged using a light-sheet microscope (LaVision Biotech UltraMicroscope, LaVision, Bielefeld, Germany) with an Olympus MVPLAPO 2x objective with 4x optical zoom (NA = 0.475) and a 5.7 mm dipping cap that is adjusted for the high refractive index of 1.56. The brain samples were imaged in an ethyl cinnamate medium to match the refractive indices and illuminated by three sheets of light bilaterally. Each light sheet was 5 µm thick, and the width was set at 30% to ensure sufficient illumination at the centroid of the sample. Laser power intensities and chromatic aberration corrections used for each laser were as follows: 10% power for 488 nm laser, 5% power for 561 nm laser with 780 nm correction, 40% power for 640 nm laser with 960 nm correction, and 100% power for 785 nm laser with 1,620 nm correction. Each sample was imaged coronally in 8 by 6 squares with 20% overlap (10,202 µm by 5,492 µm in total) and a z-step size of 15 µm (xyz resolution = 0.813 µm x 0.813 µm x 15 µm). While an excellent choice for our work, confocal microscopy offers better resolution at the expense of time. To gain a better resolution using a light-sheet microscope in select regions (eg. SNc and A13 cells), we increased the optical zoom to 6.3x.

A13 Connectome Analysis

Images were processed using ImageJ software (Schneider et al., 2012). Raw images were stitched, and a z-encoded maximum intensity projection across a 90 µm thick optical section was obtained across each brain. 90 µm sections were chosen because the 2008 Allen reference atlas images are spaced out at around 100 µm. Brains with insufficient quality in labeling were excluded from analysis (n = 1 of three sham and n = 3 of six 6-OHDA mice). Instructions for identifying YFP^+ or TH^+ cells to annotate were provided to the manual counters. YFP^+ and TH^+ cells were manually counted using the Cell Counter Plug-In (ImageJ). $mCherry^+$ fibers were segmented semi-automatically using Ilastik software (Berg et al., 2019) and quantified using particle analysis in ImageJ. Images and segmentations were imported into WholeBrain software to be registered with the 2008 Allen reference atlas (Fürth et al., 2018). The TO-PRO™-3 and TH channels were used as reference channels to register each section to a corresponding atlas image. ImageJ quantifications of cell and fiber segmentations were exported in XML formats and registered using WholeBrain software. To minimize the influence of experimental variation on the total labeling of neurons and fibers, the afferent cell counts or efferent fiber areas in each brain region were column divided by the total number found in a brain to obtain the proportion of total inputs and outputs. Connectome analyses were performed using custom R scripts (L. H. Kim et al., 2021). For interregional correlation analyses, the data were normalized to a $\log_{10}$ value to reduce variability and bring brain regions with high and low proportions of cells and fibers to a similar scale. The consistency of afferent and efferent proportions between mice was compared in a pairwise manner using Spearman's correlation (Figure S5).

Quantification of 6-OHDA mediated TH^+ cell loss.

The percentage of TH^+ cell loss was quantified to confirm 6-OHDA mediated SNc lesions. TH^+ cells within ZI, VTA and SNc areas from 90 µm thick optical brain slice images (AP: -0.655 to -3.88 mm from bregma) were manually counted by two blinded counters (n = 3 sham and n = 6 6-OHDA mice; ZI region in 2 of 6 6-OHDA mice were excluded due to presence of abnormal scarring/healing at the injection site of viruses). Subsequently, WholeBrain software (Fürth et al., 2018) was used to register and tabulate TH^+ cells in the contralesional and ipsilesional brain regions of interest. Counts obtained from the two counters were averaged per region. The percentage of TH^+ cell loss was calculated by dividing the difference in counts between contralesional and ipsilesional sides by the contralesional side count and multiplying by 100%.

Statistical analyses

All data were tested for normality using a Shapiro-Wilk test to determine the most appropriate statistical tests. The percent ipsilesional TH^+ neuron loss within the SNc as defined above using a Pearson correlation (Fougère et al., 2021) was used to ascertain the effect of the 6-OHDA lesion on behavior. A Wilcoxon rank-sum test was performed for comparisons within subjects at two timepoints where normality failed, and the central limit theorem could not be applied. The two groups were compared using an unpaired t-test with Welch's correction. A mixed model ANOVA (MM ANOVA) was used to compare the effects of group type, injection type and time. Additionally, Mauchly's test of sphericity was performed to account for differences in variability within the repeated measures design. A Greenhouse Geisser correction was applied to all ANOVAs where Mauchly's test was significant for RM and MM ANOVAs. The *post hoc* multiple comparisons were run when the respective ANOVAs reached significance using Dunnett's or Dunn's tests for repeated measures of parametric and non-parametric

tests, respectively. The pre-stimulation timepoints were used as the control time point to determine if stimulation altered behavior. A Bonferroni correction was added for *post hoc* comparisons following a MM ANOVA between groups at given time points to control for alpha value inflation. All correlations, t-tests, and ANOVAs were performed, and graphs were created using Prism version 9.3.1 (Graphpad) or SPSS (IBM, 28.0.1.0). Full statistical reporting is in Supplemental Statistics.xls.

Figures

Figures were constructed using Adobe Photoshop, Illustrator, and Biorender.

Primary Antibody	Species	Type	Supplier	Catalogue #	Dilution	Tissue Region
c-Fos	Rabbit	Polyclonal	Synaptic Systems (Göttingen, Germany)	226 003	1:1000	A13
GFP	Chicken	Polyclonal	Aves Lab (Tigard, OR)	GFP-1010	1:1000 1:5000	Whole brain A13
mCherry	Rat	Monoclonal	Invitrogen, Thermo Fisher Scientific (Waltham, MA)	M11217	1:500	Whole brain
TH	Rabbit	Polyclonal	Abcam (Cambridge, UK)	AB112	1:500 1:1000	Whole brain SNc
TH	Sheep	Polyclonal	Millipore Sigma (Burlington, MA)	AB1542	1:500	A13
Secondary Antibody			Supplier	Catalogue #	Dilution	Tissue Region
Alexa Fluor® 488 Donkey Anti-Chicken			Jackson ImmunoResearch Inc. (Westgrove, PA)	703-545-155	1:200 1:1000	Whole brain A13
Alexa Fluor® 594 Donkey Anti-Rabbit			Invitrogen, Thermo Fisher Scientific	A-21207	1:500	A13
Alexa Fluor® 647 Donkey Anti-Rabbit			Invitrogen, Thermo Fisher Scientific	A-31573	1:1000	SNc
Alexa Fluor® 647 Donkey Anti-Sheep			Invitrogen, Thermo Fisher Scientific	A-21448	1:1000	A13
Alexa Fluor® 790 Donkey Anti-Rabbit			Invitrogen, Thermo Fisher Scientific	A-11374	1:200	Whole brain
Cy™3 AffiniPure Donkey Anti-Rat			Jackson ImmunoResearch Inc.	712-165-153	1:200	Whole brain
Nuclear Stain			Supplier	Catalogue #	Dilution	Tissue Region
DAPI			Invitrogen, Thermo Fisher Scientific	D1306	1:1000	A13, SNc
TO-PRO™-3 Iodide (642/661)			Invitrogen, Thermo Fisher Scientific	T3605	1:5000	Whole brain

Table 1. List of antibodies used for immunohistochemical staining of the A13 and SNc regions, as well as the whole brain.

Day #	Instructions
1	Washed 2 x 30 minutes in PBS on a shaker at room temperature.
2	Dehydrated tissue in methanol/H_2O series of 20%, 40%, 60%, 80%, 100%, 100% (1 hour each at room temperature) then left overnight in a 66% dichloromethane/33% methanol solution.
3	Washed twice in 100% methanol at room temperature and then chilled the samples at 4°C. Bleached the samples in chilled fresh 5% H_2O_2 in methanol (1 volume 30% H_2O_2 to 5 volumes methanol), overnight at 4°C.
4	Rehydrated in methanol/water series of 80%, 60%, 40%, 20%, PBS (1 hour each at room temperature). Washed twice in PTx.2 (0.2% Triton™ X-100 in PBS). Incubated the samples in Permeabilization Solution at 37°C for 2 days.
6	Washed 3 x 1-2 hours in 0.5mM SDS/PBS at 37°C then incubated for 3 days.
9	Incubated with the primary antibody in 0.5mM SDS/PBS at 37°C for 3 days.
12	Refreshed with the primary antibody in PTx.2 at 37°C then incubated for 4 days.
17	Washed 5 x 2 hours in PTwH (0.2% Tween® 20 and 10 mg/mL Heparin stock solution in PBS) and incubated at 37°C overnight.
18	Incubated with secondary antibody in PTwH/3% Donkey Serum at 37°C for 3 days.
21	Refreshed with secondary antibody in PTwH/3% Donkey Serum at 37°C for 4 days.
25	Washed 5 x 2 hours in PTwH then incubated at 37°C overnight.
26	Dehydrated in methanol/water series of 20%, 40%, 60%, 80%, 100% (1 hour each at room temperature). Refreshed the samples with 100 % methanol and left overnight at room temperature.
27	Incubated in 66% DCM/33% methanol for 3 hours on a shaker at room temperature. Then incubated in 100% DCM (Sigma 270997-12X100ML) for 2 x 15 minutes (with shaking) to wash away methanol. Incubated samples with ethyl cinnamate for 3 hours at room temperature with shaking. Refreshed ethyl cinnamate then left at room temperature for imaging.

Table 2. Protocol for Whole Brain Clearing.

ACKNOWLEDGEMENTS
We would like to acknowledge support from Whelan and Kiss Labs and technical support from Hotchkiss Brain Institute Advanced Microscopy Platform Core Facility, Cumming School of Medicine Optogenetics Platform Core Facility and Drs. David Elliot, Jonathan Epp, Young Ou, and Lothar Resch. We acknowledge studentships from Parkinson Alberta (LHK), Parkinson Canada (LHK), Canadian Open Neuroscience Platform (AL), Cumming School of Medicine (AL, LHK), Faculty of Graduate Studies (AL, LHK), and the Faculty of Veterinary Medicine (CM, ST). This research was supported by grants to PJW provided by a Canadian Institutes of Health Research Project Grant (PJT-173511), Wings for Life, NSERC (RGPIN/04394-2019) as well as ZHTK from NSERC (RPGIN/04126-2017).

DATA AVAILABILITY
All datasets and code will be made available on a public repository.

REFERENCES

Berg S, Kutra D, Kroeger T, Straehle CN, Kausler BX, Haubold C, Schiegg M, Ales J, Beier T, Rudy M, Eren K, Cervantes JI, Xu B, Beuttenmueller F, Wolny A, Zhang C, Koethe U, Hamprecht FA, Kreshuk A. 2019. ilastik: interactive machine learning for (bio)image analysis. *Nat Methods* **16**:1226–1232.

Blomstedt P, Stenmark Persson R, Hariz G-M, Linder J, Fredricks A, Häggström B, Philipsson J, Forsgren L, Hariz M. 2018. Deep brain stimulation in the caudal zona incerta versus best medical treatment in patients with Parkinson's disease: a randomised blinded evaluation. *J Neurol Neurosurg Psychiatry* **89**:710–716.

Boix J, Padel T, Paul G. 2015. A partial lesion model of Parkinson's disease in mice--characterization of a 6-OHDA-induced medial forebrain bundle lesion. *Behav Brain Res* **284**:196–206.

Bolton AD, Murata Y, Kirchner R, Kim S-Y, Young A, Dang T, Yanagawa Y, Constantine-Paton M. 2015. A Diencephalic Dopamine Source Provides Input to the Superior Colliculus, where D1 and D2 Receptors Segregate to Distinct Functional Zones. *Cell Rep* **13**:1003–1015.

Bordia T, Perez XA, Heiss J, Zhang D, Quik M. 2016. Optogenetic activation of striatal cholinergic interneurons regulates L-dopa-induced dyskinesias. *Neurobiol Dis* **91**:47–58.

Bosson A, Boisseau S, Buisson A, Savasta M, Albrieux M. 2015. Disruption of dopaminergic transmission remodels tripartite synapse morphology and astrocytic calcium activity within substantia nigra pars reticulata. *Glia* **63**:673–683.

Braak H, Del Tredici K, Rüb U, de Vos RAI, Jansen Steur ENH, Braak E. 2003. Staging of brain pathology related to sporadic Parkinson's disease. *Neurobiol Aging* **24**:197–211.

Caire F, Ranoux D, Guehl D, Burbaud P, Cuny E. 2013. A systematic review of studies on anatomical position of electrode contacts used for chronic subthalamic stimulation in Parkinson's disease. *Acta Neurochir* **155**:1647–54; discussion 1654.

Carey RJ. 1991. Chronic L-dopa treatment in the unilateral 6-OHDA rat: evidence for behavioral sensitization and biochemical tolerance. *Brain Res* **568**:205–214.

Cenci MA, Björklund A. 2020. Animal models for preclinical Parkinson's research: An update and critical appraisal. *Prog Brain Res* **252**:27–59.

Chen F, Qian J, Cao Z, Li A, Cui J, Shi L, Xie J. 2023. Chemogenetic and optogenetic stimulation of zona incerta GABAergic neurons ameliorates motor impairment in Parkinson's disease. *iScience* **26**:107149.

Choi EA, McNally GP. 2017. Paraventricular Thalamus Balances Danger and Reward. *J Neurosci* **37**:3018–3029.

Cohen J. 1988. Statistical power analysis for the behavioral sciences New York. *NY: Academic* 54.

Costall B, Naylor RJ, Pycock C. 1976. Non-specific supersensitivity of striatal dopamine receptors after 6-hydroxydopamine lesion of the nigrostriatal pathway. *Eur J Pharmacol* **35**:276–283.

Dauer W, Przedborski S. 2003. Parkinson's disease: mechanisms and models. *Neuron* **39**:889–909.

Eaton MJ, Wagner CK, Moore KE, Lookingland KJ. 1994. Neurochemical identification of A13 dopaminergic neuronal projections from the medial zona incerta to the horizontal limb of the diagonal band of Broca and the central nucleus of the amygdala. *Brain Res* **659**:201–207.

Ferraye MU, Debû B, Fraix V, Goetz L, Ardouin C, Yelnik J, Henry-Lagrange C, Seigneuret E, Piallat B, Krack P, Le Bas J-F, Benabid A-L, Chabardès S, Pollak P. 2010. Effects of pedunculopontine nucleus area stimulation on gait disorders in Parkinson's disease. *Brain* **133**:205–214.

Fougère M, van der Zouwen CI, Boutin J, Neszvecsko K, Sarret P, Ryczko D. 2021. Optogenetic stimulation of glutamatergic neurons in the cuneiform nucleus controls locomotion in a mouse model of Parkinson's disease. *Proc Natl Acad Sci U S A* **118**. doi:10.1073/pnas.2110934118

Fürth D, Vaissière T, Tzortzi O, Xuan Y, Märtin A, Lazaridis I, Spigolon G, Fisone G, Tomer R, Deisseroth K, Carlén M, Miller CA, Rumbaugh G, Meletis K. 2018. An interactive framework for whole-brain maps at cellular resolution. *Nat Neurosci* **21**:139–149.

Glajch KE, Fleming SM, Surmeier DJ, Osten P. 2012. Sensorimotor assessment of the unilateral

6-hydroxydopamine mouse model of Parkinson's disease. *Behav Brain Res* **230**:309–316.
Glickstein M, Stein J. 1991. Paradoxical movement in Parkinson's disease. *Trends Neurosci* **14**:480–482.
Goldowitz D. 2010. Allen Reference Atlas. A Digital Color Brain Atlas of the C57BL/6J Male Mouse - by H. W. Dong. *Genes, Brain and Behavior*. doi:10.1111/j.1601-183x.2009.00552.x
Gradinaru V, Mogri M, Thompson KR, Henderson JM, Deisseroth K. 2009. Optical deconstruction of parkinsonian neural circuitry. *Science* **324**:354–359.
Gut NK, Winn P. 2015. Deep Brain Stimulation of Different Pedunculopontine Targets in a Novel Rodent Model of Parkinsonism. *Journal of Neuroscience*. doi:10.1523/jneurosci.3646-14.2015
Haery L, Deverman BE, Matho KS, Cetin A, Woodard K, Cepko C, Guerin KI, Rego MA, Ersing I, Bachle SM, Kamens J, Fan M. 2019. Adeno-Associated Virus Technologies and Methods for Targeted Neuronal Manipulation. *Front Neuroanat* **13**:93.
Hamani C, Moro E, Lozano AM. 2011. The pedunculopontine nucleus as a target for deep brain stimulation. *J Neural Transm* **118**:1461–1468.
Hansen HH, Roostalu U, Hecksher-Sørensen J. 2020. Whole-brain three-dimensional imaging for quantification of drug targets and treatment effects in mouse models of neurodegenerative diseases. *Neural Regeneration Res* **15**:2255–2257.
Hoffman BJ, Palkovits M, Paiak K, Hamson SR, Mezey É. 1997. Regulation of Dopamine Transporter mRNA Levels in the Central Nervous System In: Goldstein DS, Eisenhofer G, McCarty R, editors. Advances in Pharmacology. Academic Press. pp. 202–206.
Hormigo S, Zhou J, Castro-Alamancos MA. 2020. Zona Incerta GABAergic Output Controls a Signaled Locomotor Action in the Midbrain Tegmentum. *eNeuro* **7**. doi:10.1523/ENEURO.0390-19.2020
Hughes AJ, Ben-Shlomo Y, Daniel SE, Lees AJ. 1992. What features improve the accuracy of clinical diagnosis in Parkinson's disease: a clinicopathologic study. *Neurology* **42**:1142–1146.
Iancu R, Mohapel P, Brundin P, Paul G. 2005. Behavioral characterization of a unilateral 6-OHDA-lesion model of Parkinson's disease in mice. *Behav Brain Res* **162**:1–10.
Jagmag SA, Tripathi N, Shukla SD, Maiti S, Khurana S. 2015. Evaluation of Models of Parkinson's Disease. *Front Neurosci* **9**:503.
Keith B. J. Franklin MA, Paxinos G. 2008. The Mouse Brain in Stereotaxic Coordinates, Compact: The Coronal Plates and Diagrams. Elsevier Science.
Kimbrough A, Lurie DJ, Collazo A, Kreifeldt M, Sidhu H, Macedo GC, D'Esposito M, Contet C, George O. 2020. Brain-wide functional architecture remodeling by alcohol dependence and abstinence. *Proc Natl Acad Sci U S A* **117**:2149–2159.
Kim L, Chomiak T, Tran MA, Tam S, McPherson C, Eaton SEA, Ou Y, Kiss ZHT, Whelan PJ. 2021. Global remodelling of afferent and efferent projections of the A13 region following unilateral nigrostriatal degeneration using 6-hydroxydopamineNeuroscience Meeting Planner. Presented at the Society for Neuroscience.
Kim LH, Chomiak T, Tran M, Tam S, McPherson C, Eaton SEA, Ou Y, Resch L, Kiss ZHT, Whelan PJ. 2021. Substantia nigra degradation results in widespread changes in medial zona incerta afferent and efferent connectomics.
Kim LH, Sharma S, Sharples SA, Mayr KA, Kwok CHT, Whelan PJ. 2017. Integration of Descending Command Systems for the Generation of Context-Specific Locomotor Behaviors. *Front Neurosci* **11**:581.
Kish SJ, Tong J, Hornykiewicz O, Rajput A, Chang L-J, Guttman M, Furukawa Y. 2008. Preferential loss of serotonin markers in caudate versus putamen in Parkinson's disease. *Brain* **131**:120–131.
Koblinger K, Jean-Xavier C, Sharma S, Füzesi T, Young L, Eaton SEA, Kwok CHT, Bains JS, Whelan PJ. 2018. Optogenetic Activation of A11 Region Increases Motor Activity. *Front Neural Circuits* **12**:86.
Konnova EA, Translational Neurogenetics Unit, Wallenberg Neuroscience Center, Lund University, Lund, Sweden, Swanberg M, Translational Neurogenetics Unit, Wallenberg Neuroscience Center, Lund University, Lund, Sweden. 2018. Animal models of Parkinson's diseaseParkinson's Disease: Pathogenesis and Clinical Aspects. Codon Publications. pp. 83–106.

Kravitz AV, Freeze BS, Parker PRL, Kay K, Thwin MT, Deisseroth K, Kreitzer AC. 2010. Regulation of parkinsonian motor behaviours by optogenetic control of basal ganglia circuitry. *Nature* **466**:622–626.
Lane EL, Cheetham SC, Jenner P. 2006. Does contraversive circling in the 6-OHDA-lesioned rat indicate an ability to induce motor complications as well as therapeutic effects in Parkinson's disease? *Exp Neurol* **197**:284–290.
Lee CS, Schulzer M, Mak E, Hammerstad JP, Calne S, Calne DB. 1995. Patterns of asymmetry do not change over the course of idiopathic parkinsonism: implications for pathogenesis. *Neurology* **45**:435–439.
Li L-X, Li Y-L, Wu J-T, Song J-Z, Li X-M. 2022. Glutamatergic Neurons in the Caudal Zona Incerta Regulate Parkinsonian Motor Symptoms in Mice. *Neurosci Bull* **38**:1–15.
Lim S-Y, Fox SH, Lang AE. 2009. Overview of the extranigral aspects of Parkinson disease. *Arch Neurol* **66**:167–172.
Li S, Shi Y, Kirouac GJ. 2014. The hypothalamus and periaqueductal gray are the sources of dopamine fibers in the paraventricular nucleus of the thalamus in the rat **8**:136.
Lizarraga KJ, Jagid JR, Luca CC. 2016. Comparative effects of unilateral and bilateral subthalamic nucleus deep brain stimulation on gait kinematics in Parkinson's disease: a randomized, blinded study. *J Neurol* **263**:1652–1656.
Li Z, Rizzi G, Tan KR. 2021. Zona incerta subpopulations differentially encode and modulate anxiety. *Sci Adv* **7**:eabf6709.
Magno LAV, Tenza-Ferrer H, Collodetti M, Aguiar MFG, Rodrigues APC, da Silva RS, Silva J do P, Nicolau NF, Rosa DVF, Birbrair A, Miranda DM, Romano-Silva MA. 2019. Optogenetic Stimulation of the M2 Cortex Reverts Motor Dysfunction in a Mouse Model of Parkinson's Disease. *J Neurosci* **39**:3234–3248.
Masini D, Kiehn O. 2022. Targeted activation of midbrain neurons restores locomotor function in mouse models of parkinsonism. *Nat Commun* **13**:504.
Matsuura K, Kabuto H, Makino H, Ogawa N. 1997. Pole test is a useful method for evaluating the mouse movement disorder caused by striatal dopamine depletion. *J Neurosci Methods* **73**:45–48.
Matzuk MM, Saper CB. 1985. Preservation of hypothalamic dopaminergic neurons in Parkinson's disease. *Ann Neurol* **18**:552–555.
Meredith GE, Rademacher DJ. 2011. MPTP mouse models of Parkinson's disease: an update. *J Parkinsons Dis* **1**:19–33.
Messanvi F, Eggens-Meijer E, Roozendaal B, van der Want JJ. 2013. A discrete dopaminergic projection from the incertohypothalamic A13 cell group to the dorsolateral periaqueductal gray in rat. *Front Neuroanat* **7**:41.
Mitrofanis J. 2005. Some certainty for the "zone of uncertainty"? Exploring the function of the zona incerta. *Neuroscience* **130**:1–15.
Mitrofanis J, Mikuletic L. 1999. Organisation of the cortical projection to the zona incerta of the thalamus. *J Comp Neurol* **412**:173–185.
Mok D, Mogenson GJ. 1986. Contribution of zona incerta to osmotically induced drinking in rats. *Am J Physiol* **251**:R823–32.
Moon HC, Won SY, Kim EG, Kim HK, Cho CB, Park YS. 2018. Effect of optogenetic modulation on entopeduncular input affects thalamic discharge and behavior in an AAV2-α-synuclein-induced hemiparkinson rat model. *Neurosci Lett* **662**:129–135.
Moriya S, Yamashita A, Masukawa D, Setoyama H, Hwang Y, Yamanaka A, Kuwaki T. 2020. Involvement of A13 dopaminergic neurons located in the zona incerta in nociceptive processing: a fiber photometry study. *Mol Brain* **13**:60.
Moro E, Hamani C, Poon Y-Y, Al-Khairallah T, Dostrovsky JO, Hutchison WD, Lozano AM. 2010. Unilateral pedunculopontine stimulation improves falls in Parkinson's disease. *Brain* **133**:215–224.
Negishi K, Payant MA, Schumacker KS, Wittmann G, Butler RM, Lechan RM, Steinbusch HWM, Khan AM, Chee MJ. 2020. Distributions of hypothalamic neuron populations coexpressing tyrosine

hydroxylase and the vesicular GABA transporter in the mouse. *J Comp Neurol* **528**:1833–1855.
Noga BR, Whelan PJ. 2022. The Mesencephalic Locomotor Region: Beyond Locomotor Control. *Front Neural Circuits* **16**:884785.
Nonnekes J, Bereau M, Bloem BR. 2020. Freezing of Gait and Its Levodopa Paradox. *JAMA Neurol* **77**:287–288.
Nonnekes J, Snijders AH, Nutt JG, Deuschl G, Giladi N, Bloem BR. 2015. Freezing of gait: a practical approach to management. *Lancet Neurol* **14**:768–778.
Ogawa N, Hirose Y, Ohara S, Ono T, Watanabe Y. 1985. A simple quantitative bradykinesia test in MPTP-treated mice. *Res Commun Chem Pathol Pharmacol* **50**:435–441.
Ogundele OM, Lee CC, Francis J. 2017. Thalamic dopaminergic neurons projects to the paraventricular nucleus-rostral ventrolateral medulla/C1 neural circuit. *The Anatomical Record*. doi:10.1002/ar.23528
Okun MS, Foote KD. 2010. Parkinson's disease DBS: what, when, who and why? The time has come to tailor DBS targets. *Expert Rev Neurother* **10**:1847–1857.
Ossowska K. 2019. Zona incerta as a therapeutic target in Parkinson's disease. *Journal of Neurology*. doi:10.1007/s00415-019-09486-8
Peoples C, Spana S, Ashkan K, Benabid A-L, Stone J, Baker GE, Mitrofanis J. 2012. Photobiomodulation enhances nigral dopaminergic cell survival in a chronic MPTP mouse model of Parkinson's disease. *Parkinsonism Relat Disord* **18**:469–476.
Perez-Lloret S, Barrantes FJ. 2016. Deficits in cholinergic neurotransmission and their clinical correlates in Parkinson's disease. *NPJ Parkinsons Dis* **2**:16001.
Périer C, Tremblay L, Féger J, Hirsch EC. 2002. Behavioral consequences of bicuculline injection in the subthalamic nucleus and the zona incerta in rat. *J Neurosci* **22**:8711–8719.
Périer C, Vila M, Féger J, Agid Y, Hirsch EC. 2000. Functional activity of zona incerta neurons is altered after nigrostriatal denervation in hemiparkinsonian rats. *Exp Neurol* **162**:215–224.
Perović M, Mladenović A, Rakić L, Ruzdijić S, Kanazir S. 2005. Increase of GAP-43 in the rat cerebellum following unilateral striatal 6-OHDA lesion. *Synapse* **56**:170–174.
Plaha P, Khan S, Gill SS. 2008. Bilateral stimulation of the caudal zona incerta nucleus for tremor control. *J Neurol Neurosurg Psychiatry* **79**:504–513.
Power BD, Mitrofanis J. 1999. Evidence for extensive inter-connections within the zona incerta in rats. *Neurosci Lett* **267**:9–12.
Renier N, Wu Z, Simon DJ, Yang J, Ariel P, Tessier-Lavigne M. 2014. iDISCO: a simple, rapid method to immunolabel large tissue samples for volume imaging. *Cell* **159**:896–910.
Requejo C, López-de-Ipiña K, Ruiz-Ortega JÁ, Fernández E, Calvo PM, Morera-Herreras T, Miguelez C, Cardona-Grifoll L, Cepeda H, Ugedo L, Lafuente JV. 2020. Changes in Day/Night Activity in the 6-OHDA-Induced Experimental Model of Parkinson's Disease: Exploring Prodromal Biomarkers. *Front Neurosci* **14**:590029.
Roostalu U, Salinas CBG, Thorbek DD, Skytte JL, Fabricius K, Barkholt P, John LM, Jurtz VI, Knudsen LB, Jelsing J, Vrang N, Hansen HH, Hecksher-Sørensen J. 2019. Quantitative whole-brain 3D imaging of tyrosine hydroxylase-labeled neuron architecture in the mouse MPTP model of Parkinson's disease. *Dis Model Mech* **12**. doi:10.1242/dmm.042200
Ryan MB, Bair-Marshall C, Nelson AB. 2018. Aberrant Striatal Activity in Parkinsonism and Levodopa-Induced Dyskinesia. *Cell Rep* **23**:3438–3446.e5.
Ryczko D, Cone JJ, Alpert MH, Goetz L, Auclair F, Dubé C, Parent M, Roitman MF, Alford S, Dubuc R. 2016. A descending dopamine pathway conserved from basal vertebrates to mammals. *Proc Natl Acad Sci U S A* **113**:E2440–9.
Sahel J-A, Boulanger-Scemama E, Pagot C, Arleo A, Galluppi F, Martel JN, Delaux A, de Saint Aubert J-B, de Montleau C, Gutman E, Audo I, Duebel J, Picaud S, Dalkara D, Blouin L, Taiel M, Roska B. 2021. Partial recovery of visual function in a blind patient after optogenetic therapy. *Nat Med* **27**:1223–1229.
Sanders TH, Jaeger D. 2016. Optogenetic stimulation of cortico-subthalamic projections is sufficient to

ameliorate bradykinesia in 6-ohda lesioned mice. *Neurobiol Dis* **95**:225–237.
Sanghera MK, Anselmo-Franci J, McCann SM. 1991. Effect of Medial Zona Incerta Lesions on the Ovulatory Surge of Gonadotrophins and Prolactin in the Rat. *Neuroendocrinology*. doi:10.1159/000125931
Sanghera MK, Grady S, Smith W, Woodward DJ, Porter JC. 1991. Incertohypothalamic A13 dopamine neurons: effect of gonadal steroids on tyrosine hydroxylase. *Neuroendocrinology* **53**:268–275.
Scatton B, Javoy-Agid F, Rouquier L, Dubois B, Agid Y. 1983. Reduction of cortical dopamine, noradrenaline, serotonin and their metabolites in Parkinson's disease. *Brain Res* **275**:321–328.
Schneider CA, Rasband WS, Eliceiri KW. 2012. NIH Image to ImageJ: 25 years of image analysis. *Nat Methods* **9**:671–675.
Schwarting RK, Bonatz AE, Carey RJ, Huston JP. 1991. Relationships between indices of behavioral asymmetries and neurochemical changes following mesencephalic 6-hydroxydopamine injections. *Brain Res* **554**:46–55.
Sharma S, Kim LH, Mayr KA, Elliott DA, Whelan PJ. 2018. Parallel descending dopaminergic connectivity of A13 cells to the brainstem locomotor centers. *Sci Rep* **8**:7972.
Shaw VE, Spana S, Ashkan K, Benabid A-L, Stone J, Baker GE, Mitrofanis J. 2010. Neuroprotection of midbrain dopaminergic cells in MPTP-treated mice after near-infrared light treatment. *J Comp Neurol* **518**:25–40.
Simola N, Morelli M, Carta AR. 2007. The 6-hydroxydopamine model of Parkinson's disease. *Neurotox Res* **11**:151–167.
Sita LV, Elias CF, Bittencourt JC. 2007. Connectivity pattern suggests that incerto-hypothalamic area belongs to the medial hypothalamic system **148**:949–969.
Stanford Optogenetics Resource Center. n.d. https://web.stanford.edu/group/dlab/cgi-bin/graph/chart.php
Stefani A, Lozano AM, Peppe A, Stanzione P, Galati S, Tropepi D, Pierantozzi M, Brusa L, Scarnati E, Mazzone P. 2007. Bilateral deep brain stimulation of the pedunculopontine and subthalamic nuclei in severe Parkinson's disease. *Brain* **130**:1596–1607.
Stott SRW, Barker RA. 2014. Time course of dopamine neuron loss and glial response in the 6-OHDA striatal mouse model of Parkinson's disease. *Eur J Neurosci* **39**:1042–1056.
Thevathasan W, Debu B, Aziz T, Bloem BR, Blahak C, Butson C, Czernecki V, Foltynie T, Fraix V, Grabli D, Joint C, Lozano AM, Okun MS, Ostrem J, Pavese N, Schrader C, Tai C-H, Krauss JK, Moro E, Movement Disorders Society PPN DBS Working Groupin collaboration with the World Society for Stereotactic and Functional Neurosurgery. 2018. Pedunculopontine nucleus deep brain stimulation in Parkinson's disease: A clinical review. *Mov Disord* **33**:10–20.
Thiele SL, Warre R, Nash JE. 2012. Development of a unilaterally-lesioned 6-OHDA mouse model of Parkinson's disease. *J Vis Exp*. doi:10.3791/3234
Tsang E, Orlandini C, Sureka R, Crevenna AH, Perlas E, Prankerd I, Masferrer ME, Gross CT. 2021. Induction of flight via midbrain projections to the cuneiform nucleus. *bioRxiv*. doi:10.1101/2021.12.21.473683
Ungerstedt U. 1971. Striatal dopamine release after amphetamine or nerve degeneration revealed by rotational behaviour. *Acta Physiol Scand Suppl* **367**:49–68.
Valverde S, Vandecasteele M, Piette C, Derousseaux W, Gangarossa G, Aristieta Arbelaiz A, Touboul J, Degos B, Venance L. 2020. Deep brain stimulation-guided optogenetic rescue of parkinsonian symptoms. *Nat Commun* **11**:2388.
Venkataraman A, Hunter SC, Dhinojwala M, Ghebrezadik D, Guo J, Inoue K, Young LJ, Dias BG. 2021. Incerto-thalamic modulation of fear via GABA and dopamine. *Neuropsychopharmacology* **46**:1658–1668.
Wang X, Chou X-L, Zhang LI, Tao HW. 2020. Zona Incerta: An Integrative Node for Global Behavioral Modulation. *Trends Neurosci* **43**:82–87.
Wardas J, Ossowska K, Wolfarth S. 1988. Evidence for the independent role of GABA synapses of the zona incerta-lateral hypothalamic region in haloperidol-induced catalepsy. *Brain Res* **462**:378–382.
Yoon HH, Nam M-H, Choi I, Min J, Jeon SR. 2020. Optogenetic inactivation of the entopeduncular

nucleus improves forelimb akinesia in a Parkinson's disease model. *Behav Brain Res* **386**:112551.
Yoon HH, Park JH, Kim YH, Min J, Hwang E, Lee CJ, Suh J-KF, Hwang O, Jeon SR. 2014. Optogenetic inactivation of the subthalamic nucleus improves forelimb akinesia in a rat model of Parkinson disease. *Neurosurgery* **74**:533–40; discussion 540–1.
Zetterström T, Herrera-Marschitz M, Ungerstedt U. 1986. Simultaneous measurement of dopamine release and rotational behaviour in 6-hydroxydopamine denervated rats using intracerebral dialysis. *Brain Res* **376**:1–7.
Zhan Y, Wu H, Liu L, Lin J, Zhang S. 2021. Organic solvent-based tissue clearing techniques and their applications. *J Biophotonics* **14**:e202000413.
Zhao Z-D, Chen Z, Xiang X, Hu M, Xie H, Jia X, Cai F, Cui Y, Chen Z, Qian L, Liu J, Shang C, Yang Y, Ni X, Sun W, Hu J, Cao P, Li H, Shen WL. 2019. Zona incerta GABAergic neurons integrate prey-related sensory signals and induce an appetitive drive to promote hunting. *Nat Neurosci* **22**:921–932.
Zweig RM, Jankel WR, Hedreen JC, Mayeux R, Price DL. 1989. The pedunculopontine nucleus in Parkinson's disease. *Ann Neurol* **26**:41–46.

SUPPLEMENTARY MATERIAL

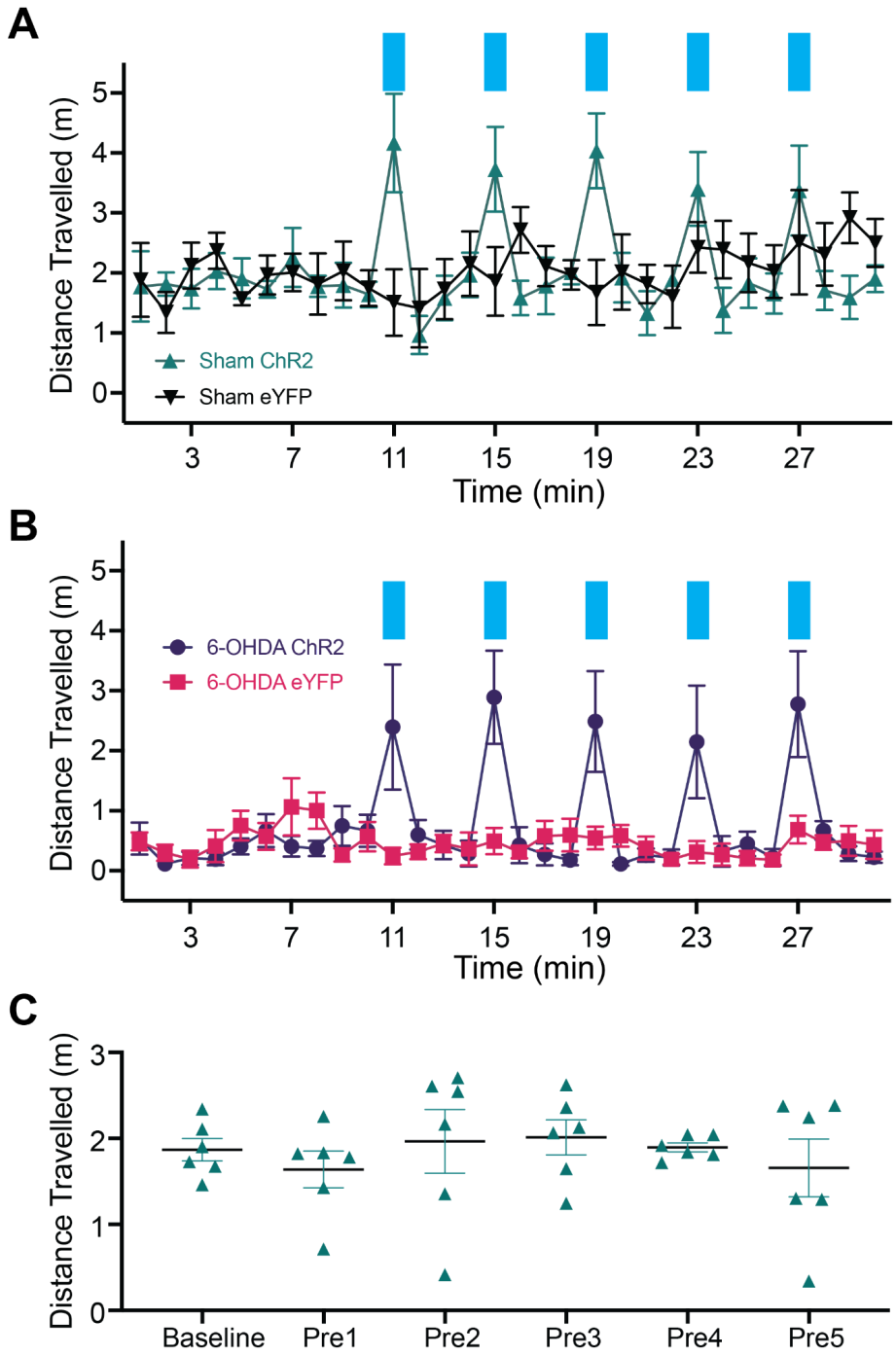

Figure S1. Time course of open field locomotion distance travelled over 30 minutes. (A-B) 30-minute open field experiment group averages for sham **(A)** and 6-OHDA **(B)** animals with photoactivation plotted as 1-minute bins of distance travelled. Blue bars indicate 1-minute trials with photoactivation. (**C)** Locomotion distance travelled for the six sham ChR2 animals at baseline and at the five pre-timepoints compared using a 1-way RM ANOVA ($F_{5,25}$ = 0.486, P = .783). Data indicate mean ± SEM bars.

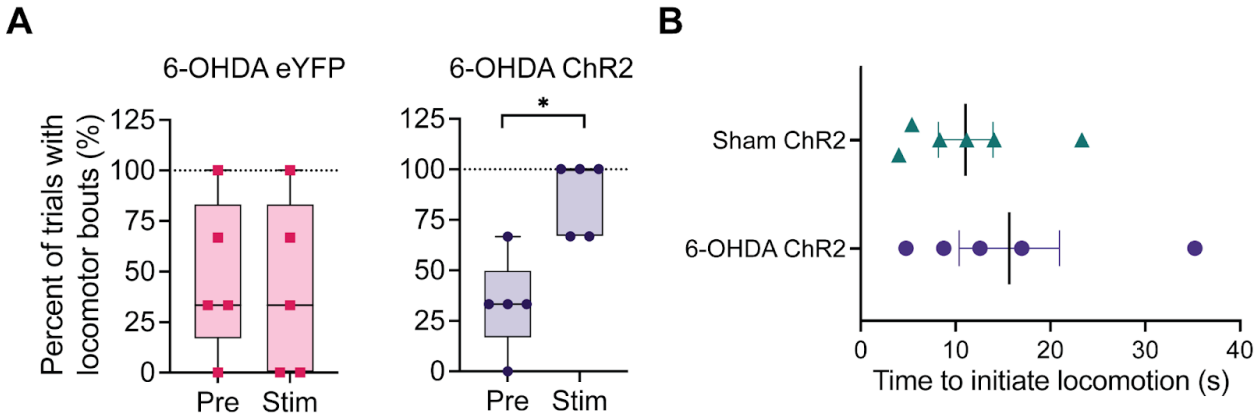

Figure S2. Characterization of A13 region photoactivation temporal dynamics on locomotion initiation. (A) Percent of trials where there was at least one bout of locomotion. Data are plotted as box and whiskers with the horizontal line through the box indicating the group median, interquartile range indicated by the limits of the box, and group minimum and maximum indicated by the whiskers. **(B)** The average time for the ChR2 group animals to begin locomotion after the onset of photoactivation. Means plotted with error bars indicating ± SEM. Asterisks indicate significant comparisons using the Wilcoxon signed-rank test: ** $P \leq 0.05$.

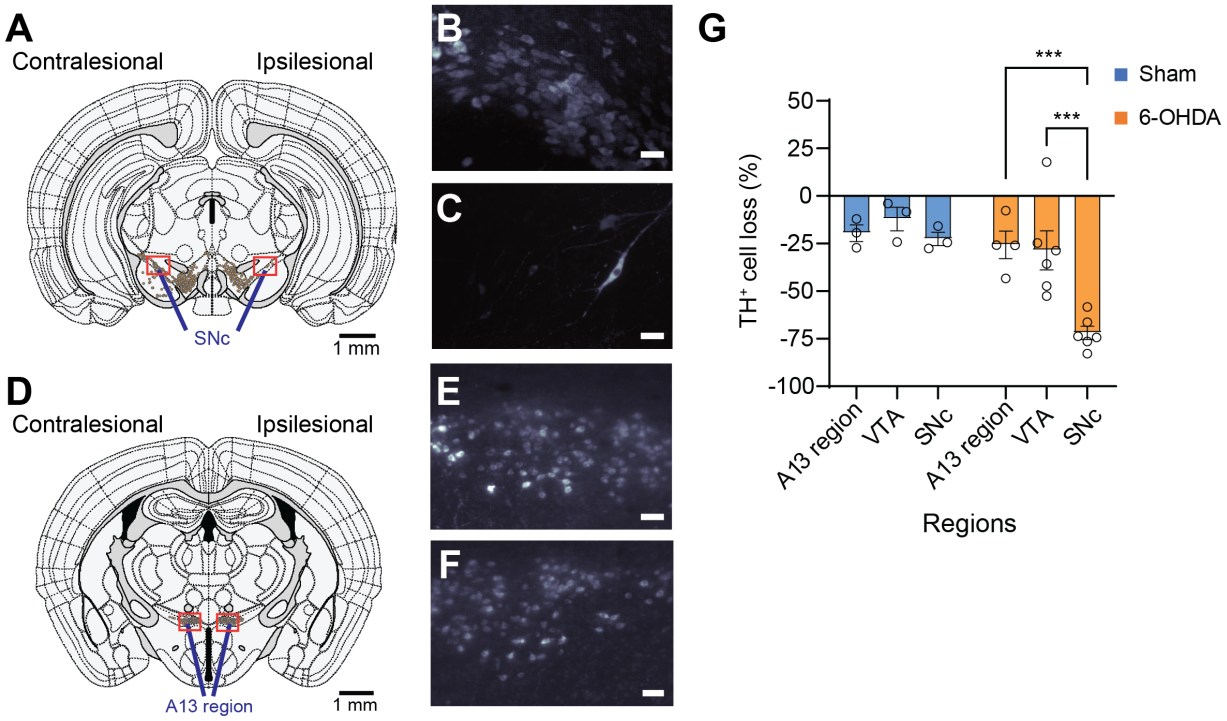

Figure S3. **Preservation of TH$^+$ A13 cells in Parkinsonian mouse models.**
Representative slices of SNc (AP: -3.08 mm, **A**) and A13 region (AP: -1.355 mm, **D**) following registration with WholeBrain software 64. Full 3D brain is available (see Movie S4). There was a lack of TH$^+$ SNc cells following 6-OHDA injections at the MFB **(A)**. **(B, C)** Zoomed sections (90 µm thickness) of red boxes in panel A in left to right order. Meanwhile, TH$^+$ VTA cells were preserved bilaterally. In addition, TH$^+$ A13 cells were present ipsilesional to 6-OHDA injections **(D)**. **(E, F)** Zoomed sections (90 µm thickness) of red boxes in panel D in left to right order. Scale bars are 50 µm. When calculating the percentage of TH$^+$ cell loss normalized to the intact side, there was a significant interaction between the condition group and brain regions (repeated measures two-way ANOVA with *post hoc* Bonferroni pairwise, sham: n = 3, 6-OHDA: n = 6) **G**). 6-OHDA treated mice showed a significantly greater percentage of TH$^+$ cell loss in SNc compared to VTA and A13 region (VTA vs. SNc: $P = 0.005$; A13 region vs. SNc: $P = 0.029$). In contrast, sham showed no significant difference in TH$^+$ cell loss across SNc, VTA and A13 region regions ($P > 0.05$). *$P \leq 0.05$, and **$P \leq 0.01$. Scale bars are 50 µm unless otherwise indicated.

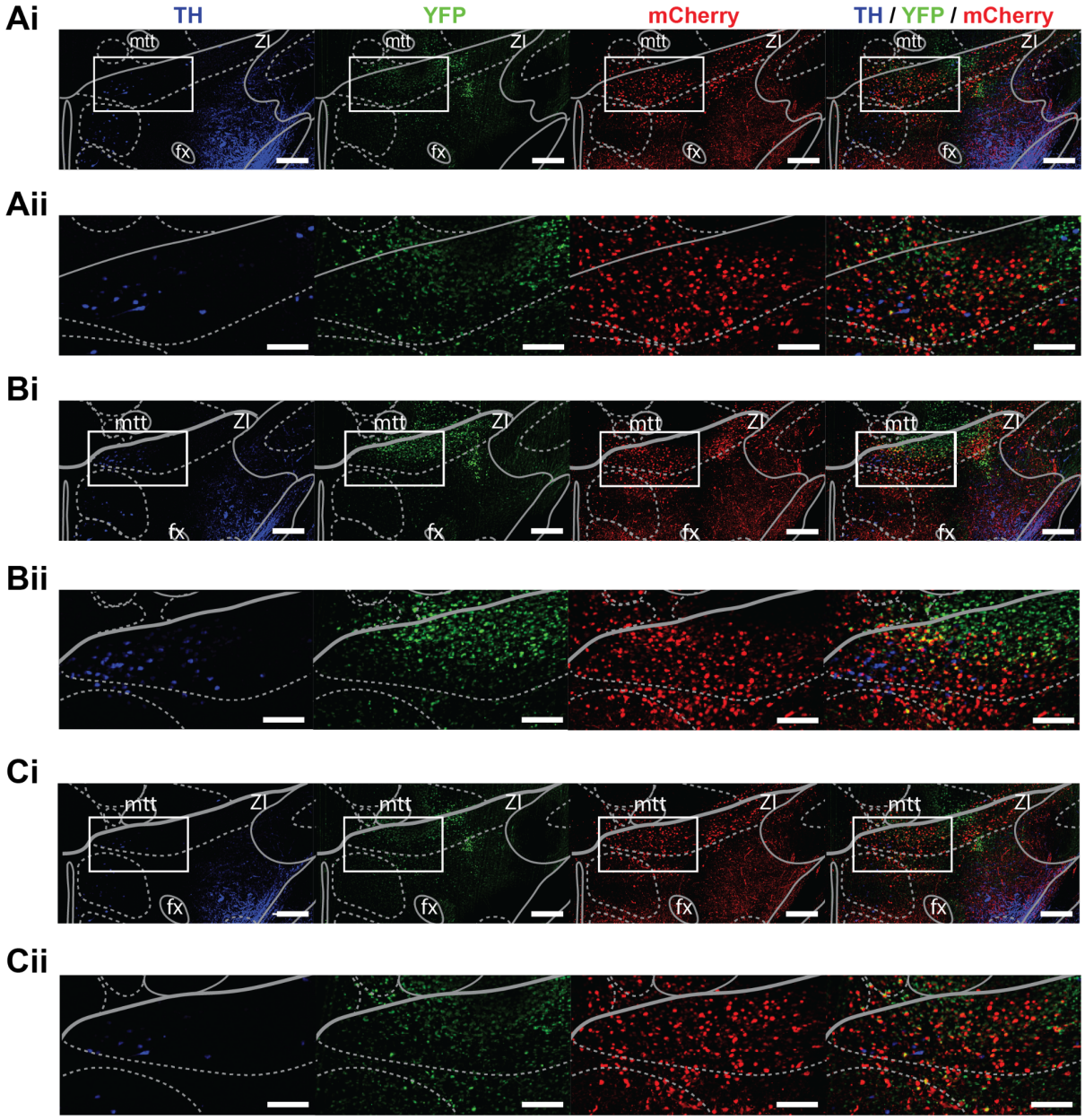

Figure S4. Example of the injection core in a sham brain for viral tracers and the rostral and caudal spread to the injection site (A13). Viral tracers (AAV8-CamKII-mCherry and AAVrg-CAG-GFP) were mixed 50:50. Light-sheet images around the injection site were obtained with 2x objective, 6.3x optical zoom, and a z-step size of 2 µm (xyz resolution = 0.477 µm x 0.477 µm x 2 µm). Background filtering (median value of 20 pixels and Gaussian smoothing with a sigma value of 10) was performed in ImageJ software 1 and visualized in IMARIS 9.8 (Belfast, United Kingdom). 2008 Allen reference atlas images were overlaid on top of 90 µm maximum intensity projections taken from IMARIS 9.8 (Belfast, United Kingdom):-1.26 mm **(A)**, -1.36 mm **(B)**, and -1.46 mm **(C)**. Zoomed in sections of each white rectangular area at each coordinate (rows '**i**') are displayed below for each fluorophore (rows '**ii**'). Scale bars for rows 'i' are 200 µm and for rows 'ii are 100 µm.

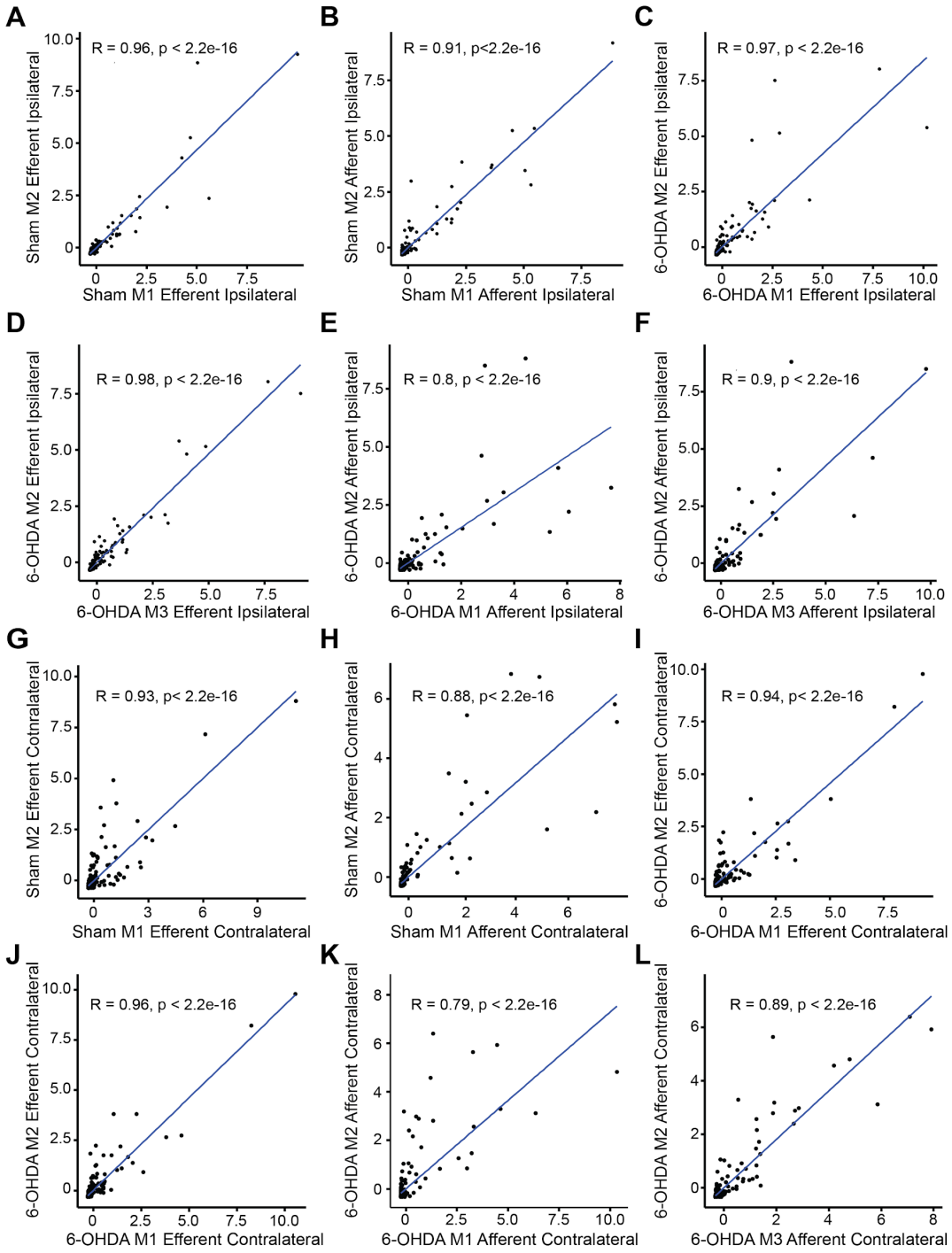

Figure S5. The consistency of afferent and efferent proportions across mice was compared in a pairwise manner. An experimental variation on the total labeling of neurons and fibers was minimized by dividing the afferent cell counts or efferent fiber areas in each brain region by the total number found in a brain to obtain the proportion of total inputs and outputs. Using Spearman's correlation analysis, we found afferent and efferent proportions across animals to be consistent among each other with an average correlation of 0.91 (SEM = 0.02). M1 = mouse #1, M2 = mouse #2, M3 = mouse #3.

Movie S1. Photoactivation of the A13 region in a 6-OHDA model mouse producing increased locomotion in the OFT (2x speed).

Movie S2. Photoactivation of the A13 region in a sham mouse producing increased locomotion in the OFT (2x speed).

Movie S3. Photoactivation of the A13 region during the pole test in a 6-OHDA model mouse decreases pole descent time (0.5x speed).

Movie S4. Video showing TH staining following whole brain imaging and staining in a 6-OHDA model mouse brain. Focus on TH expression in the A13 and SNc regions.